CHARACTERIZATION OF BROADBAND OPTICAL FUNCTIONALITY OF FREEFORM OPTICS

by

Jonathan Christian Koerber

A dissertation submitted to the faculty of
The University of North Carolina at Charlotte
in partial fulfillment of the requirements
for the degree of Doctor of Philosophy in
Optical Science and Engineering

Charlotte

2022

Approved by:

_____
Dr. Thomas J. Suleski

_____
Dr. Glenn D. Boreman

_____
Dr. Gregory J. Gbur

_____
Dr. Steven R. Patterson

ABSTRACT

JONATHAN CHRISTIAN KOERBER. Characterization of Broadband Optical Functionality of Freeform Optics. (Under the direction of DR. THOMAS J. SULESKI)

Freeform optics, broadly described as optical elements with at least one surface lacking translational or rotational symmetry, have seen increased interest due to recent advances in optical design, fabrication, and measurement. Freeform optics provide additional design freedoms and capabilities that enable greater control of wavefronts and new functionality compared to conventional optics. For these reasons, freeform optics are receiving great interest for imaging, metrology, illumination, and many other applications. However, most freeform elements are designed for monochromatic light sources, especially in the case of transmissive optics. Studies on the advantages, disadvantages, and applications of freeforms with broadband sources have been limited to some illumination systems and to reflective systems which are inherently achromatic.

The primary goal of this dissertation is to characterize examples of transmissive freeform optics in applications where broadband optical functionality is not currently enabled or where freeform optics enable enhanced broadband functionality. Results are addressed through three articles. The first article presents a broadband variable transmission sphere based on freeform Alvarez lenses to facilitate Fizeau interferometry across a broad range of f-numbers and source wavelengths. The second article demonstrates the use of additional freeform design freedoms to reduce undesirable retrace errors in broadband variable transmission spheres. The third article reports on the design and performance of freeform transmissive elements for compact and efficient broadband laser beam shaping. These three articles illustrate advantages and challenges for the use of freeform optics in broadband optical systems.

ACKNOWLEDGMENTS

DEDICATION

This dissertation and all my progress and achievement in life is dedicated first and foremost to my Lord and Savior Jesus Christ. By His grace this dissertation is also dedicated to my dear parents, Jim and Michelle Koerber. Their willing sacrifice of time and energy to raise and teach myself and my siblings at home has enabled us all to succeed in life in many ways. This dissertation could not be possible without their encouragement to push forward through the easy and hard times in life. Soli Deo Gloria.

TABLE OF CONTENTS

LIST OF FIGURES

LIST OF TABLES

LIST OF ABBREVIATIONS

BVTS   broadband variable transmission sphere

EPD   entrance pupil diameter

FWHM   full-width half-maximum

IR   infrared

LWIR   long-wave infrared

MCE   multi-configuration editor

MWIR   mid-wave infrared

NIR   near infrared

PV   peak-to-valley

RMS   root-mean-square

ROC   radius of curvature

TS   transmission sphere

CHAPTER 1: INTRODUCTION

1.1 Background and Motivation: Broadband Optical Systems

Optical systems designed to function over large ranges of source wavelengths are advantageous for many applications and light sources but requires additional design considerations. For example, many applications benefit from the use of multiple source wavelengths for increasing the amount of available information (i.e. for imaging [1-21] and material detection [22-27]). In order to obtain high-fidelity information, the optical systems must be able to function similarly for each source wavelength. Additional applications for broadband optical systems include laser beam shaping [6, 15, 28-30], material interactions [31-33], illumination [34-38], communications [39, 40], medical applications [3, 8, 41] and many others.

It is beneficial to distinguish between two types of optical systems that function across wide wavelength ranges. Achromatic optical systems have the same function at the 'same place' or configuration for two or more source wavelengths [5-21, 26, 28-30, 42, 43]. Broadband systems which are non-achromatic leverage changes in system configuration or geometry to function for two or more source wavelengths separately [44-47]. In simpler terms, all achromatic systems are broadband, but not all broadband systems are achromatic, as illustrated by Figures 1.1-1.3.
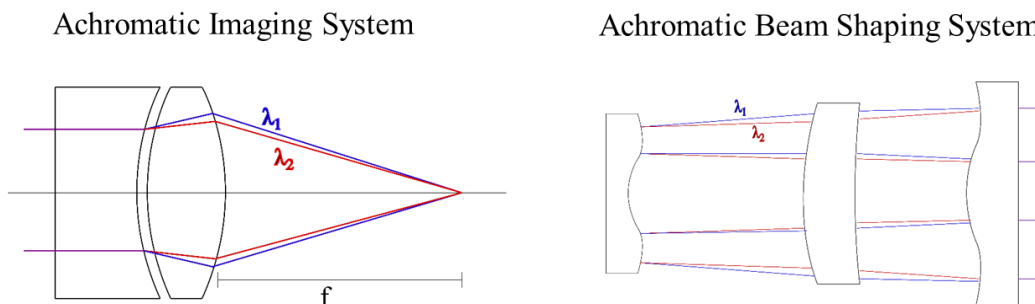
Fig. 1.1: Examples of achromatic optical systems.
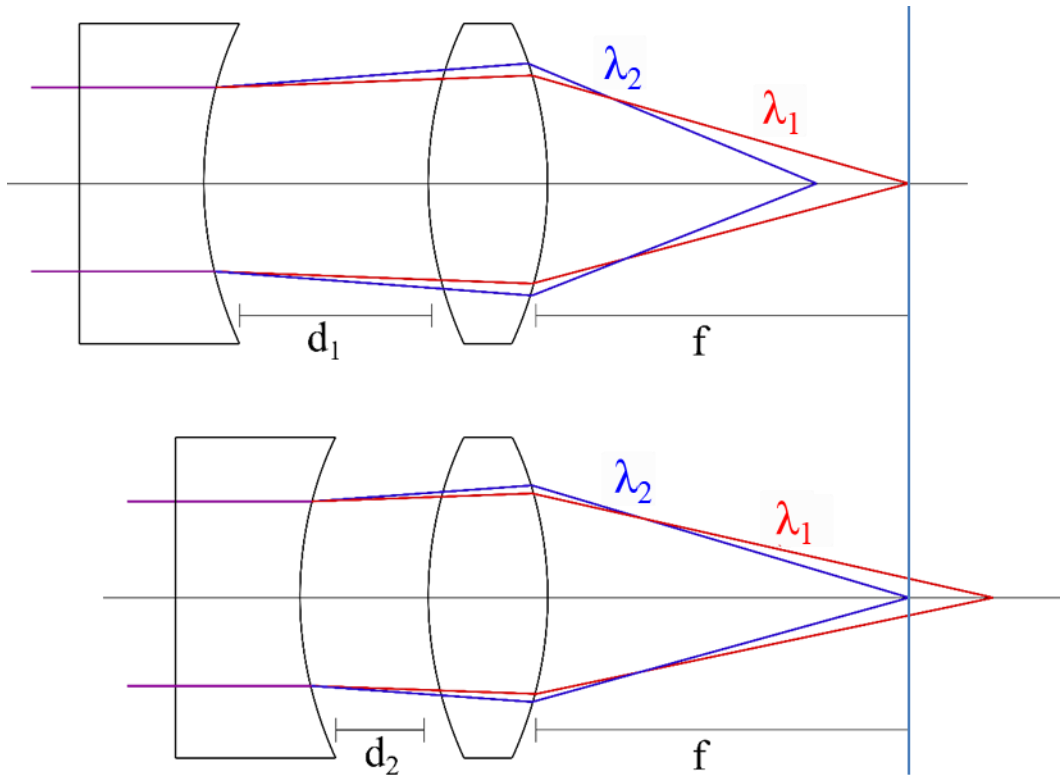
Fig. 1.2: Examples of non-achromatic broadband imaging system.
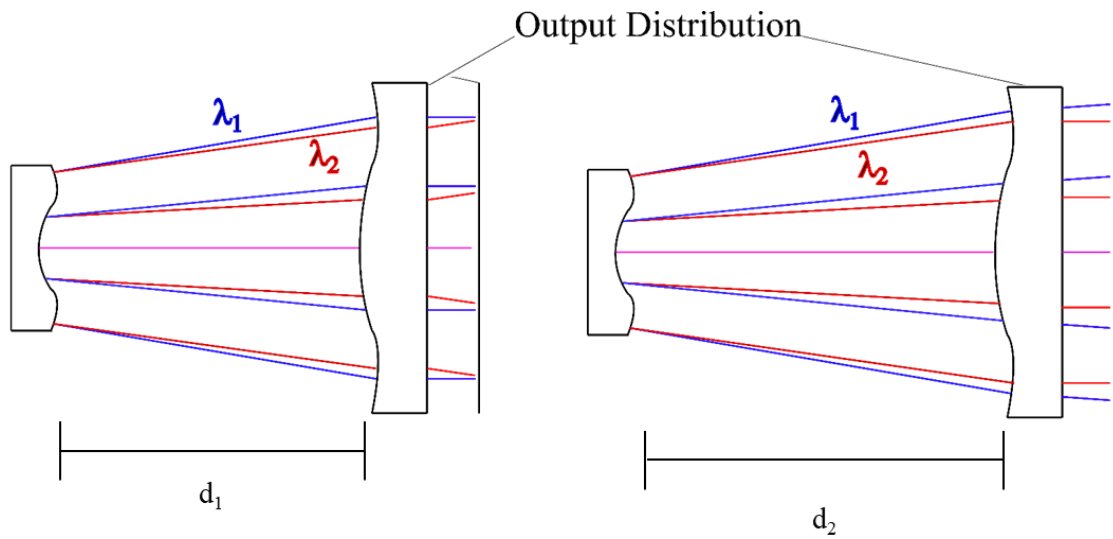
Fig. 1.3: Examples of non-achromatic broadband beam-shaping system.

Broadband functionality can reduce the number of systems or components required in a lab or application space where multiple source wavelengths are used. For example, instead of having one

imaging system for each light source, a single broadband system would function for multiple light sources and therefore replace multiple imaging systems across the range of source wavelengths.

1.2 Background and Motivation: Freeform Optics

Freeform optics are a growing field of optical components which utilize at least one surface without translational or rotational symmetry [48-50]. Advances in design software, manufacturing technology, and surface characterization techniques are enabling and encouraging the development of freeform systems. Freeform optics have been studied for imaging, metrology, illumination, laser beam shaping, and other design spaces with a wide variety of benefits. Freeform optical systems can enable greater control of wavefronts and increased functionality when compared to conventional optical systems. For example, the Alvarez and Lohmann lenses are classic freeform systems in which a variable focal length is achieved by relative lateral translation between two freeform surfaces [51-58]. Beam shaping systems benefit from freeform surfaces which can enable unique or variable output distributions [34-37, 59-64]. Further, freeform systems can facilitate changes in system geometries that enable more compact systems or reduce the number of components needed [65].

1.3 Broadband Freeform Optical Systems

To date, many freeform optical systems have been designed for monochromatic sources. Notable exceptions are reflective freeform systems which are inherently achromatic [49, 66-70] and transmissive illumination systems which are inherently broadband [34-38, 59, 63, 64]. A goal of this dissertation is to investigate and characterize broadband functionality for transmissive

freeform optical systems. Conventional and commercially available systems provide motivation for exploration of transmissive freeform optical systems capable of broadband functionality. Comparisons of the performance of broadband freeform systems to conventional systems are presented, and the advantages, disadvantages, and general operating principles of broadband freeform optical systems are discussed.

Two specific applications of broadband freeform optical systems are explored in this dissertation. The first investigates use of the variable focal length freeform Alvarez lens to realize variable transmission spheres for use in Fizeau interferometry. The resulting broadband variable transmission sphere (BVTS) system enables both broadband functionality and wavefront outputs not currently available with conventional transmission spheres. Broadband functionality for transmission spheres in Fizeau interferometry has been suggested previously for limited wavelength ranges [21, 71-73]. Variable focal length transmission spheres have also been suggested, but as rotationally translated diffractive versions of the Alvarez lens (also known as a Moiré lens) that are limited in wavelength [74-77]. In contrast, BVTS systems are refractive and functionally broadband for any source wavelength for which the component material is transmissive. Further, the BVTS systems can match any transmission sphere f-number within the designed f/# range. Advantages of the BVTS concept include reducing the number of transmission spheres needed to be kept on hand when changing source wavelengths or surfaces under test.

Achromatic beam shapers with non-radially symmetric outputs are considered as a second type of broadband freeform system. Beam shaping employs the concept of energy conservation during design to enable redistribution of source irradiance and phase into additional prescribed patterns [44, 78, 79]. A primary example of laser beam shaping is the redistribution of a Gaussian input beam to a uniform 'flat-top' energy distribution [78, 80, 81]. Conventional laser beam shaping

systems use combinations of transmissive aspheric [15, 29, 79], hybrid refractive and diffractive [82-84], or freeform surfaces [59, 69, 85, 86]. Conventional transmissive laser beam shaping systems have reported non-radial output distributions such as 'roof-top' and square distributions [87, 88]. However, these conventional transmissive beam shapers require additional components such as cylindrical lenses or masks (which result in a loss of energy) after a Gaussian beam is redistributed to a uniform circle [87-93], or are diffractive systems and that are inherently monochromatic [31, 81, 82, 94-99]. Freeform transmissive beam shapers for non-radially symmetric outputs have been demonstrated but are limited in source wavelength ranges [60-62, 100-103]. Broadband and achromatic laser beam shaping have been demonstrated by wavelength-tunable systems based on liquid deformation [104], or the addition of a spherical lens to correct chromatic aberrations in aspheric systems [6, 15, 28-30], or by changing the longitudinal separation of aspheric surfaces in a classic afocal laser beam shaper [44]. In contrast to previous systems, this dissertation explores freeform refractive laser beam shapers in both broadband and achromatic configurations to enable non-radially symmetric outputs without a loss of energy due to masking or the need for added optical components.

1.4 Dissertation Outline

Chapter 2 introduces the principles behind transmission spheres in Fizeau interferometry and their limitations in f/# and source wavelength and introduces the BVTS system as an alternative solution. The broadband capabilities of Alvarez lenses are discussed along with the conceptual advantages of a variable focal length system in Fizeau interferometers. Introductory design methodologies, designs, and simulations are presented, along with initial performance metrics for two BVTS systems. The wavefront error performance for the BVTS systems are demonstrated for

a 4" entrance pupil diameter across a broad range of source wavelengths (0.6328 to 10.6 µm) and f-numbers. Simulated measurement results for ideal spherical surfaces in a Fizeau interferometer are also presented. The initial results were aberrated, particularly for shorter source wavelengths, and did not match measurement performance targets except for the long wave infrared case. The potential benefits and disadvantages of the BVTS systems are discussed in detail.

Chapter 3 expands on the limitations of the BVTS systems identified in Chapter 2 by considering the nature of retrace error and the challenges of freeform surfaces within transmission spheres. The retrace errors induced by the two initial BVTS systems are quantified, and an updated optimization method is presented and used to design a third BVTS system with reduced retrace error. Simulation results for the third BVTS system are presented and evaluated in comparison to the earlier results reported in Chapter 2. Significant performance improvements are seen across all wavelengths and f-numbers for the updated BVTS system compared to the initial two designs.

Chapter 4 considers broadband laser beam shaping using freeform surfaces to generate output distributions with non-radial symmetry. Differences in design methodologies for freeform non-radially symmetric outputs are discussed and applied for both afocal and focal freeform systems. Dimensions and uniformity of output distributions are considered as performance metrics and applied to a series of freeform achromatic laser beam shapers designed for different spectral ranges. The resulting performance metrics are compared with respect to wavelength and design method.

Lastly, Chapter 5 summarizes the results of Chapters 2 through 4 and provides comparisons between systems and the general principles, advantages, and disadvantages of the demonstrated

broadband freeform optical systems. Suggestions for future research and other applications are also presented.

CHAPTER 2: BROADBAND VARIABLE TRANSMISSION SPHERE FOR FIZEAU
INTERFEROMETRY

2.1 Introduction

2.1.1 Transmission Spheres in Fizeau Interferometry

Fizeau interferometry is an industry standard for measuring the form of optical sur-faces. This non-contact characterization approach uses high-quality transmission spheres to create high-quality spherical wavefronts designed to match the shapes of nominally spherical test surfaces [71, 105-110]. Optical path differences due to variations in the shape of the test surface result in constructive and destructive interference fringes on a detector when the wavefront reflected from the test surface is recombined with a reference wavefront. The appropriate f-number transmission sphere must be chosen such that the center of curvature of the surface under test and the focal plane of the transmission sphere are aligned, allowing the test wavefront to match the test surface. The cost of multiple transmission spheres can be significant, and time is required to switch components and re-calibrate if consecutive surfaces under test are not within the same curvature range or have multiple curvatures on one surface, such as aspheres or freeforms [49, 111-113]. Most transmission spheres are designed to operate at a single design wavelength, and a change in source wavelength requires a change in the transmission sphere used or an alternative transmission sphere, such as an adaptive optical element [21, 105]. An alternative to the conventional spherical transmission sphere would be a system capable of variable focal length (and f-number), allowing for the measurement of a broader range of surface curvatures with one system. In this work, we explore a method for replacing a set of fixed transmission spheres with a variable focus element, with a goal of reducing the required inventory of transmission spheres needed in laboratories performing these types of measurements. We find that, particularly for source wavelengths in the infrared, the

accuracy of this approach is sufficient that a variable focus element may provide a practical option for optical form measurements in future interferometric systems.

Variable-focal-length optical systems as transmission spheres have been previously proposed and tested for use in Fizeau interferometers [14, 74, 76, 77, 114, 115]. Bielke designed and tested a variable-focal-length Moirè lens, capable of variation in focal length by equal and opposite rotation of two elements [74, 76, 77]. Bielke's system is diffractive and therefore mono-chromatic, requiring additional systems for other source wavelengths. Others have explored adaptive optics such as liquid lenses to achieve nominally achromatic systems of variable focal length as transmission spheres, but these are narrowly limited in the range of achievable f-numbers and achromatic source ranges [14].

2.1.2 Alvarez Lenses

In this work, we explore the Alvarez varifocal lens as a single replacement for multiple spherical transmission spheres. Alvarez and Lohmann varifocal lenses are classic examples of systems which vary in focal length through relative lateral shifts of paired freeform surfaces [51-54, 56-58, 116]. In the simplest case, the freeform surfaces can be described by Equation 2.1:

$$z(x, y) = A(\frac{x^3}{3} + xy^2) \tag{2.1}$$

Where the z-axis is the direction of light propagation and the x-axis is the axis along which the freeform elements are translated in equal and opposite directions with respect to each other. A is the surface sag coefficient and is related to the system's optical power. Additional polynomial coefficients can be added in optimization steps to reduce surface depth modulation and wavefront aberrations. It has previously been shown that A is related to the focal length, f, of the system at the lateral shift, d, and the index of refraction of the freeform elements, $n(\lambda)$ [51].

$$f = \left[4Ad(n(\lambda)-1)\right]^{-1} \qquad (2.2)$$

An Alvarez lens can transform a planar wavefront into a range of converging or diverging wavefronts and thus is variable in f-number (Figure 1).
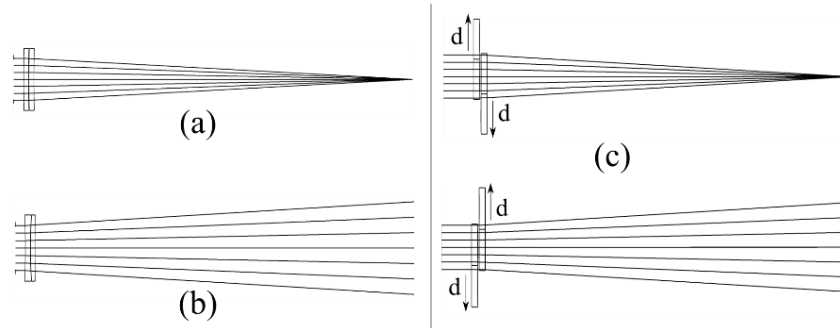
Fig. 2.1: Converging (a) and diverging (b) transmission spheres, and an Alvarez lens (c) shifted to match (a) and (b).

In addition to the variable f-number enabled by the Alvarez lens, there is a unique form of broadband functionality. While not inherently achromatic, an Alvarez lens can achieve the same focal lengths for different source wavelengths through small shifts of the freeform elements (Fig. 2.1).
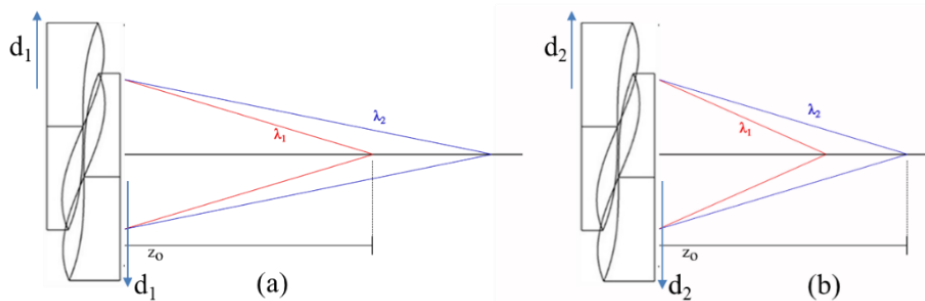
Fig. 2.2: Broadband functionality: Alvarez lens shifted such that (a) design wavelength is in focus and (b) non-design wavelength is now in focus.

The analytical designs discussed here assume no separation between the freeform surfaces, but in reality a small air gap is needed so that the surfaces do not collide during translation.

Transmission spheres require a reference surface such that the planar wavefront from the source is divided in amplitude [117]. The reference wavefront reflects off the reference surface

and propagates to the detector. The remainder of the wavefront incident on the reference surface propagates to the test surface, reflects off the test surface, and propagates back through the transmission sphere to the detector where it interferes with the reference wavefront. Spherical transmission spheres are designed such that the surface closest to the part under test has a radius of curvature (ROC) equal to its focal length, resulting in exit rays normal to the reference surface. A BVTS system has no spherical surfaces to use as reference surfaces, so a separate flat surface of one of the plano-freeform elements of the BVTS can be used.

A practical advantage of the BVTS is its ability to generate a null interferogram without significantly shifting the test part along the optical axis. Laterally shifting the BVTS components until the f-number matches the test surface eliminates the need to translate the test surface so that its center of curvature and the transmission sphere focal plane are coincident, which is required when using a fixed f-number transmission sphere (Fig. 2.3). Translating the test part along the optical axis as needed for a fixed f-number transmission sphere results in a loss of surface coverage. This is illustrated in Fig. 2.3 and numerically represented in Table 2.1 for the example BVTS system described in Section 2.2.3.
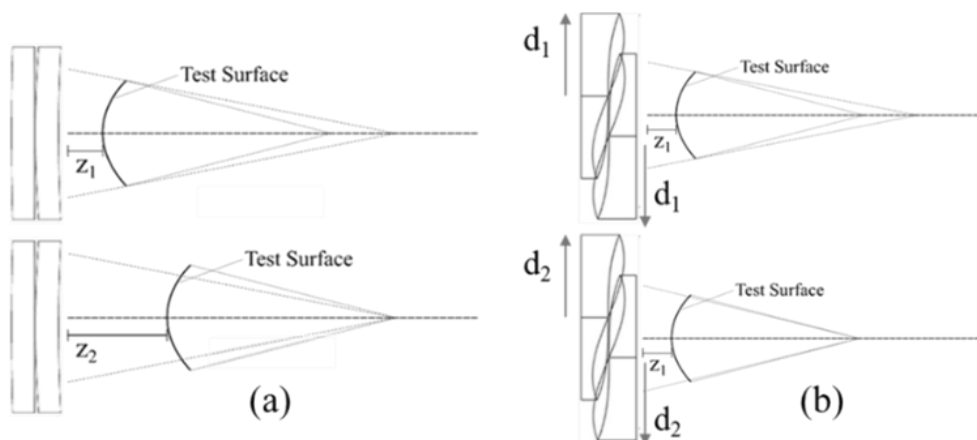
Fig. 2.3: Translation of: (a) test surface along optical axis or (b) Alvarez elements.

Table 2.1: Optical element locations for wavefront matching surface curvature of first example BVTS system (Section 2.3.2, 632.8 nm source).

	z (mm)		d (mm)
f-number	TS	BVTS	BVTS 1st Element
80	127.9	25.0	7.504
45	71.9	25.2	13.283
32	55.9	25.1	17.035
25	39.9	25.0	23.745
15	23.9	25.0	39.181

Two BVTS systems were first designed in Zemax OpticStudio™ and then used in VirtualLab Fusion™ to simulate measurements of spherical surfaces in a Fizeau interferometer. In the following section, we present the design process and simulation setup.

2.2 Design of BVTS Systems

2.2.1 System Parameters

Zygo's Transmission Sphere Selection Guide was used to determine general system parameters of BVTS systems designed in Zemax OpticStudio™ [105]. The entrance pupil diameter (EPD) from this set is 101.6 mm. The optical systems in the selection guide range from ±f/15 to ±f/80. For this investigation, visible to long-wave infrared laser wavelengths were chosen (0.6328, 1.55, 3.39, and 10.6 μm). Zinc sulfide (ZnS) was chosen as the optical material for this study because of its transmissivity and relatively low dispersion over the entire band of interest. Other materials could also be considered based on manufacturability and transmissivity across smaller wavelength ranges, for example zinc selenide or germanium for mid- to long-wave IR sources, and fused silica or quartz for ultraviolet to near-IR sources.

Element diameters larger than the EPD are needed to accommodate the EPD and the required lateral shifts of the Alvarez lens. First, light passing through the EPD must have a clear path through the BVTS without reflection off the edge walls when the BVTS system is shifted to the

fastest f-number configuration (the largest shift distance). Second, the relation between element shift distance, *d,* and surface coefficient *A* in Equation 2.2 and manufacturing challenges such as surface sag and slope must be considered to reduce the necessary air gap between the two freeform surfaces. For this study, element diameters of 190.5 mm and a maximum shift, *d,* of 44.45 mm were used, with a 25.4 mm center thickness of each element.

The BVTS system was optimized in Zemax OpticStudio™ with the goals of: (1) a diffraction-limited spot for each f-number and source wavelength combination and (2) less than $\lambda/10$ of peak-to-valley (PV) and root-mean-square (RMS) wavefront errors. These initial optimization metrics were chosen based on the performance targets set for conventional transmission spheres in the Zygo Transmission Sphere Section Guide [105]. The Multi-Configuration Editor (MCE) tool was used to optimize the BVTS system. In the MCE tool, system parameters can be duplicated in copies of the first system such that surface parameters are fixed but optical element locations and parameters such as f-number can be different in each configuration. By doing so, we can optimize the BVTS system for each f-number and source wavelength at the same time, achieving the best overall results for the system in each of the BVTS configurations. We now consider two different BVTS designs based on the Alvarez lens geometry.

2.2.2 BVTS Example 1

To achieve better performance, additional low-order polynomials can be added to the basic freeform surface in Equation 2.3 and allowed to vary during optimization. The resulting freeform surface coefficients are shown in Table 2.2.

$$z(x, y) = A(\frac{x^3}{3} + xy^2) + Bx^2y + Cxy + Dy^2 + Ex \tag{2.3}$$

Table 2.2: Surface coefficients for BVTS Example 1 (Equation 2.3).

A mm^{-2}	B mm^{-2}	C mm^{-1}	D mm^{-1}	E
3.06901×10^{-6}	-5.56451×10^{-13}	-7.67717×10^{-8}	5.19685×10^{-5}	-0.02

Diffraction-limited spot sizes were achieved for the system, except for the visible source at f/15. All slower f-numbers achieved diffraction-limited spot sizes. PV and RMS wavefront results with respect to centroid (with piston and tilt subtracted) are shown in Table 2.3, indicating acceptable performance at IR wavelengths.

Table 2.3: Wavefront errors for BVTS example 1 (Equation 2.3).

	Source Wavelength (µm)					Source Wavelength (µm)			
	0.6328	1.55	3.39	10.6		0.6328	1.55	3.39	10.6
f-number	PV (waves)				f-number	RMS (waves)			
f/15	0.504	0.192	0.087	0.027	f/15	0.085	0.033	0.015	0.006
f/25	0.340	0.129	0.058	0.017	f/25	0.051	0.019	0.009	0.003
f/35	0.273	0.102	0.046	0.014	f/35	0.041	0.015	0.007	0.002
f/45	0.244	0.088	0.040	0.012	f/45	0.040	0.014	0.006	0.002
f/80	0.350	0.123	0.054	0.015	f/80	0.048	0.017	0.007	0.002

2.2.3 BVTS Example 2

Grewe et al. reviewed earlier designs from Smilie to analyze aberrations induced by an Alvarez system [56, 58]. They identified a method to compensate for aberrations induced by the freeform surfaces by adding fourth-order polynomial terms to the surface. It is of interest to compare the performance of this system with the BVTS in the previous section. Beginning with the BVTS system from the previous section and following Grewe's analysis, x^4, x^2y^2, x^2, and y^4 terms were added (Equation 2.4) and the system was optimized for spot size and PV wavefront error as before. Table 2.4 outlines the resulting surface coefficients for this second BVTS example.

$$z(x, y) = A(\frac{x^3}{3} + xy^2) + Bx^2y + Cxy + Dy^2 + Ex + Fx^4 + Gx^2y^2 + Hy^4 + Ix^2 \qquad (2.4)$$

Table 2.4: Surface coefficients for BVTS example 2 (Equation (2.4)).

A mm^{-2}	B mm^{-2}	C mm^{-1}	D mm^{-1}	E	F mm^{-3}	G mm^{-3}	H mm^{-3}	I mm^{-1}
3.12039 $\times 10^{-6}$	-6.01610 $\times 10^{-18}$	3.74566 $\times 10^{-12}$	-5.99074 $\times 10^{-6}$	-9.3728 $\times 10^{-3}$	5.8794 $\times 10^{-12}$	3.52603 $\times 10^{-11}$	1.36198 $\times 10^{-9}$	-2.29134 $\times 10^{-7}$

Diffraction-limited spot sizes were met for the IR sources with more ray distribution symmetry than the original BVTS. Results for the second BVTS example are shown in Table 2.5. PV and RMS wavefront results (with respect to centroid) are smaller and decrease more consistently for slower f-numbers than the first BVTS design. Further, results at 1.55 μm miss the PV target only for the f/15 configuration. RMS values are negligible for all source wavelengths.

Table 2.5: Wavefront errors for BVTS example 2 (Equation (2.4)).

	Source Wavelength (μm)					Source Wavelength (μm)			
	0.6328	1.55	3.39	10.6		0.6328	1.55	3.39	10.6
f-number	PV (waves)				f-number	RMS (waves)			
f/15	0.447	0.172	0.078	0.024	f/15	0.109	0.043	0.019	0.006
f/25	0.270	0.101	0.045	0.014	f/25	0.058	0.022	0.010	0.003
f/35	0.237	0.087	0.039	0.011	f/35	0.051	0.019	0.008	0.002
f/45	0.227	0.083	0.037	0.011	f/45	0.049	0.018	0.008	0.002
f/80	0.222	0.080	0.036	0.010	f/80	0.049	0.018	0.008	0.002

2.3 Fizeau Interferometer Simulation

A model for a Fizeau interferometer with 101.6 mm EPD was configured in VirtualLab Fusion™ for characterizing and comparing the performance of a BVTS system and spherical transmission spheres, as shown in Figure 2.4 [118-121]. In our model, a collimated source was directed towards a beam-splitter with the transmitted light incident on the transmission sphere and transmitted to the test surface. Light reflected from the transmission sphere and from the test surface was reflected to the detector by the beam-splitter. An aperture was placed on the BVTS planar surface nearest to the test piece to block unwanted light from reflecting through the system at the edges of the BVTS when configured to the maximum lateral shift.
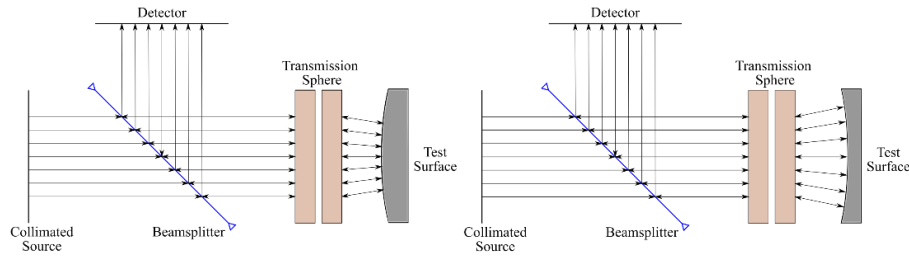
Fig. 2.4: Diagram view of Fizeau interferometer in VirtualLab Fusion™ for convex and concave surfaces.

All components except for the transmission sphere and test surface were 'ideal' components, as defined in VirtualLab Fusion™ to simplify the simulations. At the detector, the reference and test wavefronts interfere with each other, resulting in an interferogram corresponding to variations in the surface with respect to the reference wavefront. Measurements of ideal test surfaces were simulated using both BVTS systems, and the phase data from the interferograms were exported as ASCII files for analysis.

A MATLAB® script was written to import and evaluate phase data from the simulated interferograms obtained in VirtualLab Fusion™. Two phase-unwrapping algorithms were used for comparison to ensure results were reasonably unwrapped [122, 123]. Unwrapping the phase and converting to optical path differences results in a 'height map' corresponding to deviations between the wavefront and the test surface. Since both the surface parameters and the ideal wavefront parameters are known, we can calculate the ideal height maps, which for our perfect test surfaces and an ideal wavefront should be zero everywhere. We can find the surface measurement errors by taking the difference between the ideal case and our simulation. For this case, our height maps are also maps of the errors in the simulated results. PV and RMS magnitudes of the height maps were calculated and the ZernikeCalc MATLAB® function was used to fit Fringe Zernike polynomials to the height map for aberration analysis [124, 125]. A representative visual representation of the conversion from interferogram phase to height data is shown in Figure 2.5.
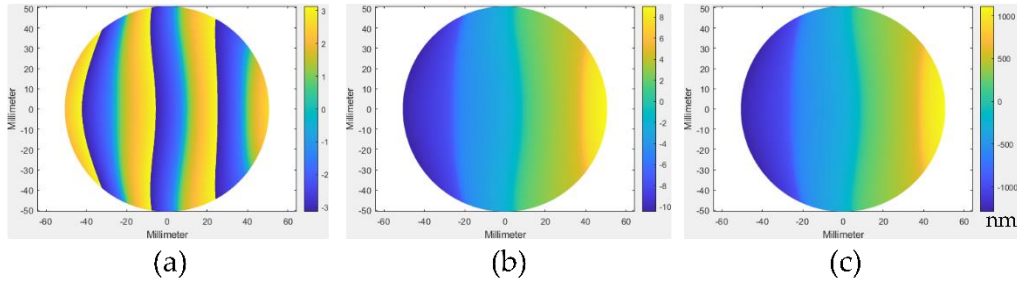
Fig. 2.5: (a) Interferogram phase, (b) unwrapped phase, and (c) phase converted to height map for 1.55 μm source, f/25 configuration, and test surface with 2.5 m radius of curvature.

2.4 Results and Discussion

2.4.1 Surface Measurements of Ideal Spherical Surfaces Using BVTS Systems

To characterize the performance of BVTS, surface measurements of perfect spherical surfaces were simulated using the Fizeau interferometer model described previously. The test surfaces were chosen to match commercially available transmission spheres [105]. Specifically, r-numbers (test surface ROC divided by test area diameter) from −81.5 to 80 were evaluated for 100 mm-diameter test surfaces. In order to measure a convex surface, the focal length of the BVTS must be greater than the ROC of the test surface, as illustrated in Figure 2.3 [105]. Since the BVTS EPD is larger than the test surface diameter, an f/80 configuration (for example) can be used to measure a convex r/80 test surface. However, obtaining a matching wavefront for a concave surface with a diverging wavefront configuration requires a focal length shorter than the test surface ROC, and thus an r/# slower than the f/# of the BVTS. The initial data are reported in terms of height maps and PV error magnitudes. As before, the target is PV $\leq \lambda/10$.

The first four Fringe Zernike polynomial aberration terms (piston (Z_1), tip (Z_2), tilt (Z_3), and defocus (Z_4)) are often removed from interferometric measurement results since they can arise from system misalignments. While the results presented here are based on simulation and alignment errors do not contribute, these four aberration terms were noticeable in the results. The

presence of these lower-order aberrations is undesirable and indicates the need for an alternative optimization metric.

Since Zernike polynomials are orthogonal, the data can be filtered by subtracting individual terms from the height data obtained from simulation [124, 125]. The first four Zernike terms were subtracted from the height data, and the RMS and PV errors of the filtered height data were calculated to isolate higher-order aberrations. RMS errors were consistently sub-nanometer in scale and therefore negligible for both BVTS systems. Table 2.6 shows the filtered PV results for both systems.

Table 2.6: PV wavefront errors for ideal surface measurements (filtered).

BVTS Example 1					BVTS Example 2			
Source Wavelength (µm)					Source Wavelength (µm)			
0.6328	1.55	3.39	10.6		0.6328	1.55	3.39	10.6
r-number	PV (waves)			**r-number**	PV (waves)			
80	0.695	0.517	0.137	0.027	80	0.831	0.512	0.060	0.008
45	0.713	0.515	0.060	0.042	45	0.776	0.579	0.279	0.032
35	0.681	0.513	0.067	0.030	35	0.735	0.599	0.221	0.041
25	0.739	0.569	0.139	0.021	25	0.958	0.560	0.189	0.033
15	0.572	0.439	0.256	0.026	15	1.174	0.417	0.214	0.044
−81.5	1.005	0.720	0.073	0.025	−81.5	0.567	0.509	0.077	0.022
−46	1.194	0.570	0.329	0.035	−46	0.738	0.516	0.206	0.047
−36	1.270	0.590	0.158	0.054	−36	1.012	0.542	0.160	0.074
−26	1.649	0.897	0.380	0.068	−26	0.887	0.616	0.157	0.019
−16	2.089	1.075	0.469	0.223	−16	1.232	0.665	0.271	0.071

The results for the 0.6328 and 1.55 µm sources did not meet our targets in either BVTS system for any r-number (r/#). The PV error exceeded $\lambda/10$ waves of aberration for all r-numbers, although RMS errors were in the order of 10^{-7} waves or less and were therefore negligible. Further, for both systems, the interferogram data possesses unwanted fringes such that accurate phase unwrapping is challenging. When the lower terms are filtered, artifacts of the fringes can be seen. Representative height data for an r/15 convex surface measurement from the first BVTS system are shown in Figure 2.6. The second BVTS example system has greater fringe density issues, likely

due to a larger tip term (Z_2), which can be seen in Figure 2.5. As the source wavelength increases, the fringe density decreases, as does the magnitude of the surface PV errors and aberrations. It is worth noting here that for the concave surfaces, the second BVTS on average, but not in each instance, has a decreased PV error. The first BVTS has smaller PV errors for positive r-numbers while the second BVTS has smaller PV errors for negative r-numbers. This indicates that the first BVTS will result in better measurements of convex surfaces while the second BVTS will be more suited to measuring concave surfaces. We note that the standard deviation of the PV error between all r-numbers was smaller for the second BVTS, resulting in less variation across all configurations.
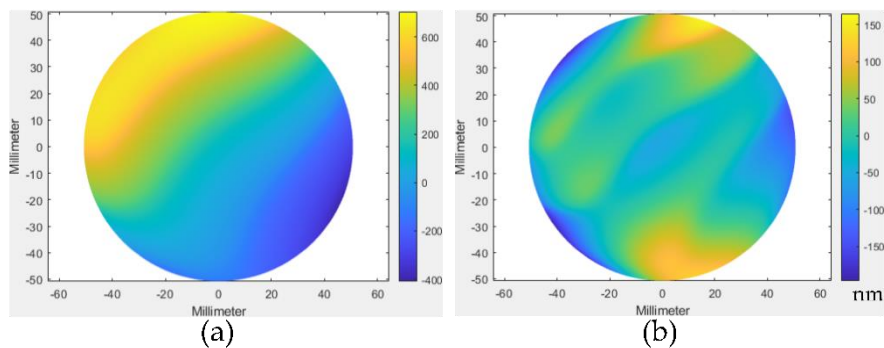
Fig. 2.6: Example of (a) unfiltered and (b) filtered height data from the first BVTS system (0.6328 µm source wavelength, r/15 surface measurement).

Systems with the 3.39 µm source wavelength met our performance targets for a handful of configurations. RMS error was once again negligible. The unfiltered PV error met the $\leq\lambda/10$ target for the r/45 convex and r/81.5 concave surface measurements with the first BVTS example system. When filtered, the first BVTS also met the PV target for the r/35 convex surface measurement. The second BVTS did not meet the PV target for any configuration, filtered or unfiltered, but the PV error was $\leq\lambda/4$ for all filtered results except the r/45 convex and r/16 concave measurements. While at this point not fully understood, it should be noted that the Fringe Zernike tip term (Z_2) for the second BVTS was exceptionally large ($\lambda/10$ to $3\lambda/5$). This term appeared to have a

significant impact on the phase unwrapping but requires further study to determine the exact impact and its possible correction.

The 10.6 μm source wavelength configuration achieved the $\leq\lambda/10$ PV target for all filtered configurations of both BVTS systems except the r/16 concave surface measurements with the first BVTS system. RMS error was once again negligible. The unfiltered case for the second BVTS did not meet the $\leq\lambda/10$ PV target for the r/25 and r/15 convex surface measurements and the r/36, r/26, and r/16 concave surface measurements. Despite aberrations, the 10.6 μm source wavelength configuration afforded the most consistent and capable results for surface measurements. The Z_2 term also dominated the surface measurement error of the second BVTS but with far less impact due to smaller amplitudes ($\lambda/50$ to $\lambda/6$).

2.4.2 Higher-Order Surface Aberrations

Aberrations that remained in the filtered data illustrate differences between the first and second BVTS systems. In the Fringe Zernike polynomial ordering, terms Z_5–Z_9 correspond to Vertical Astigmatism (Z_5), Oblique Astigmatism (Z_6), Horizontal Coma (Z_7), Vertical Coma (Z_8), and Primary Spherical (Z_9) terms. For the first BVTS system, these aberrations showed no consistent trend for r-number (Table 7). With respect to source wavelength, the overall aberration magnitudes decreased with an increase in source wavelength, as expected. The inconsistencies here may be due to fringe density issues due to the Zernike tip term present or due to inherent aberrations of the BVTS systems and doubling of these aberrations upon the test wavefront's second pass through the BVTS elements.

Table 2.7: Magnitude of higher-order aberrations for BVTS example 1 (waves/1000).

Source Wavelength (μm)	r/#	Z_5	Z_6	Z_7	Z_8	Z_9
	80	1.64	44.69	35.63	12.47	37.48
	45	56.55	59.16	44.44	38.47	37.02
0.6328	35	31.75	31.31	92.48	50.94	14.70
	25	81.56	3.64	71.79	16.11	27.83
	15	131.84	8.24	38.15	7.90	57.62
	80	0.60	17.08	7.30	9.38	15.00
	45	14.81	29.26	7.75	12.82	14.23
1.55	35	30.20	43.46	12.93	15.31	12.82
	25	13.29	47.70	52.46	19.51	31.78
	15	55.96	62.56	16.20	37.55	12.53
	80	1.66	9.83	2.58	0.47	2.09
	45	2.57	1.08	4.12	0.16	4.48
3.39	35	6.11	2.49	4.32	0.09	2.66
	25	32.75	42.36	5.77	2.84	11.75
	15	32.04	17.02	1.42	14.88	5.61
	80	0.06	0.05	0.43	0.07	0.52
	45	0.90	5.46	5.73	1.22	13.95
10.6	35	1.55	0.18	1.61	0.08	1.56
	25	2.51	0.16	1.48	0.08	0.67
	15	4.26	0.44	1.01	0.01	1.97

Table 2.8 presents the same aberrations as Table 2.7 for the second BVTS system. For this BVTS system, these aberrations also showed no consistent trend for r-number but did demonstrate a significant reduction, if not elimination, of Z_6 and Z_8. Undesirably, there was a significant increase in the other three aberrations compared to the first BVTS design. The source of this increase is not clear, but as noted in the previous section, the tip term for this system was significantly higher than in the first BVTS system and may have skewed the phase unwrapping. This indicates the need for either a different optimization method of the BVTS to reduce the tip term or a method to counteract the variable tip term present, or both. The overall aberration magnitudes also decreased with the increase in source wavelength.

Table 2.8: Magnitude of higher-order aberrations for BVTS example 2 (waves/1000).

Source Wavelength (μm)	r/#	Z_5	Z_6	Z_7	Z_8	Z_9
	80	38.03	0.01	49.38	0.00	17.19
	45	7.38	0.01	39.75	0.01	71.64
0.6328	35	1.39	0.01	49.38	0.00	60.96
	25	149.14	0.01	34.29	0.00	68.05
	15	179.65	0.02	41.32	0.00	112.80
	80	59.97	0.01	4.56	0.00	38.23
	45	27.87	0.00	8.43	0.00	15.11
1.55	35	22.48	0.00	19.67	0.00	56.48
	25	2.96	0.01	23.93	0.00	11.80
	15	6.12	0.01	47.38	0.00	41.79
	80	0.19	0.00	1.71	0.00	5.43
	45	66.11	0.00	19.02	0.00	2.46
3.39	35	63.25	0.00	38.66	0.00	8.31
	25	64.70	0.00	10.18	0.00	38.85
	15	26.70	0.00	7.52	0.00	0.77
	80	0.09	0.00	0.44	0.00	1.57
	45	0.41	0.00	0.56	0.00	1.29
10.6	35	1.16	0.00	0.93	0.00	1.36
	25	0.83	0.00	1.60	0.00	1.91
	15	4.95	0.00	12.54	0.00	4.65

2.5 Conclusions

The BVTS systems presented here may be able to replace multiple conventional transmission spheres with one Alvarez lens-based system. The results with the smallest errors in the simulated height maps were seen with IR source wavelengths in the range of f/15 to f/80. To put this in context, even if only the 10.6 μm source wavelength is considered, ten conventional transmission spheres could be replaced by a single BVTS system [105]. Additionally, the BVTS system would be functional for additional f-numbers between the conventional values. In addition to potentially replacing tens of conventional transmission spheres, a single BVTS system could possibly reduce material costs and the system alignment and calibration time needed for changing out transmission spheres. The extents of these benefits are yet to be quantified as a BVTS will include manufacturing costs and requires precision actuators for translation of the freeform elements.

Applications which do not require high-precision surface measurements and can use a longer source wavelength may be well-served by the flexibility of the wavefront curvature of the BVTS systems presented here. A refined BVTS system capable of a better performance at shorter wavelengths would greatly expand the applicability of the BVTS system concept.

BVTS systems as shown do not yet replace high-precision transmission spheres when tight tolerances are required. It will be important to further investigate the sources and impacts of the residual aberrations seen in the simulated surface measurements in BVTS systems. It may be possible to improve performance through consideration of alternative optimization metrics and methods, use of freeform surfaces with higher-order polynomials, or use of additional optical components to increase design freedoms and refined phase unwrapping.

Going forward, the source and impact of the observed errors requires further study, especially in relation to limits they may present when used to measure non-ideal surfaces. Characterizing the retrace error for ideal and aberrated surfaces would assist in further understanding of the BVTS system. Reducing the range of allowed source wavelengths and/or f-numbers would allow for alternative materials and systems which may be able to achieve improved measurement accuracy. It also remains to be seen how well BVTS systems can maintain their performance when experimentally implemented. Form and mid-spatial frequency errors resulting from freeform manufacturing processes will likely decrease performance [49]. Alignment errors will also need to be understood for a laterally shifting system in a real Fizeau interferometer.

REFERENCE LIST

14. Reichelt, Stephan and Hans Zappe. "Design of Spherically Corrected, Achromatic Variable-Focus Liquid Lenses." *Optics express*, vol. 15, no. 21, 2007, pp. 14146-54.

21. Wang, Yan et al. "Design of Multi-Wavelength Achromatic Transmission Sphere Based on Zoom Principle." *Proc. SPIE*, *Optical Metrology and Inspection for Industrial Applications VII*, vol. 11552, 2020, p. 1155217.

49. Rolland, Jannick P et al. "Freeform Optics for Imaging." *Optica*, vol. 8, no. 2, 2021, pp. 161-76.

51. Alvarez, Luis W. "Two-element variable-power spherical lens." U.S. Patent No. 3,305,294. 21 Feb. 1967.

52. Babington, James. "Alvarez Lens Systems: Theory and Applications." *Proc. SPIE, Optical Systems Design 2015: Optical Design and Engineering VI*, vol. 9626, 2015, p. 962615.

53. Barbero, Sergio. "The Alvarez and Lohmann Refractive Lenses Revisited." *Optics express*, vol. 17, no. 11, 2009, pp. 9376-90.

54. Barbero, Sergio and Jacob Rubinstein. "Adjustable-Focus Lenses Based on the Alvarez Principle." *Journal of Optics*, vol. 13, no. 12, 2011, p. 125705.

56. Grewe, Adrian et al. "Aberration Analysis of Optimized Alvarez–Lohmann Lenses." *Applied optics*, vol. 53, no. 31, 2014, pp. 7498-506.

57. Roth, Eckhard et al. "Building Challenging Optical Systems with Alvarez Lenses." *Freeform Optics*, Optical Society of America, 2019, p. FW4B. 6.

58. Smilie, Paul J et al. "Design and Characterization of an Infrared Alvarez Lens." *Optical Engineering*, vol. 51, no. 1, 2012, p. 013006.

71. Peng, Wei-Jei et al. "Design, Tolerance Analysis, Fabrication, and Testing of a 6-In. Dual-Wavelength Transmission Sphere for a Fizeau Interferometer." *Optical Engineering*, vol. 56, no. 3, 2017, p. 035105.

74. Bielke, Alexander et al. "Model-Based Calibration of an Interferometric Setup with a Diffractive Zoom-Lens." *Proc. SPIE, 2015 International Conference on Optical Instruments and Technology: Optical Systems and Modern Optoelectronic Instruments*, vol. 9618, 2015, p. 961807.

76. Bielke, Alexander et al. "Design of a Variable Diffractive Zoom Lens for Interferometric Purposes." *Optical Engineering*, vol. 56, no. 1, 2017, p. 014104.

77. Bielke, Alexander et al. "Experimental Demonstration of a Diffractive Zoom-Lens for an Interferometric Setup." *Optical Fabrication and Testing*, Optical Society of America, 2014, p. OTu4A. 3.

105. "Zygo Transmission Sphere Selection Guide." edited by ZYGO, 2014, 4. https://bit.ly/2ZNMqbK.

106. Yang, Pengqian et al. "Transmission Sphere Calibration and Its Current Limits." *Proc. SPIE, Optical Measurement Systems for Industrial Inspection VII*, vol. 8082, 2011, p. 80822L.

107. Gao, Zhishan et al. "Computer-Aided Alignment for a Reference Transmission Sphere of an Interferometer." *Optical Engineering*, vol. 43, no. 1, 2004, pp. 69-74.

108. Peng, Wei-Jei et al. "Design and Tolerance Analysis of a Transmission Sphere by Interferometer Model." Proc. SPIE, Optical System Alignment, Tolerancing, and Verification IX, vol. 9582, 2015, p. 958208.

109. Peng, Wei-Jei et al. "Mounting of Reference Surface for a Transmission Sphere." *Proc. SPIE, 8th International Symposium on Advanced Optical Manufacturing and Testing Technologies: Optical Test, Measurement Technology, and Equipment*, vol. 9684, 2016, p. 96840G.

110. Pinto, Joseph. "Transmission Spheres More Than Just a Reference Surface!" *Optifab 2003: Technical Digest*, vol. 10314, 2003, p. 1031415.

111. Dumas, Paul. "Enabling Higher Precision Freeform Surfaces Though Developments in Magnetorheological Finishing (Mrf) and Subaperture Stitching Interferometry (Ssi)." *Renewable Energy and the Environment*, Optical Society of America, 2013/11/03 2013, p. FT3B.1. *OSA Technical Digest (online)*, doi:10.1364/FREEFORM.2013.FT3B.1.

112. Murphy, Paul and Chris Supranowitz. "Freeform Testability Considerations for Subaperture Stitching Interferometry." *Proc. SPIE, Optifab*, vol. 11175, 2019, 111750Z https://doi.org/10.1117/12.2536851.

113. Supranowitz, Chris, et al. "Freeform metrology using subaperture stitching interferometry." *Proc. SPIE, Optics and Measurement International Conference 2016*, vol. 10151, 2016, 101510D.

114. Ohsaki, Yumiko et al. "Interferometer and Interferance Measurement Method." U.S. Patent No. 6,842,255. 11 Jan. 2005.

115. Suzuki, Akiyoshi and Yoshiyuki Sekine. "Interferometer and Interferance Measurement Method." U.S. Patent No. 7,106,455. 12 Sep. 2006.

116. Lohmann, Adolf W. "A New Class of Varifocal Lenses." *Applied optics*, vol. 9, no. 7, 1970, pp. 1669-71.

117. Burge, James H. "Fizeau Interferometry for Large Convex Surfaces." *Proc. SPIE, Optical Manufacturing and Testing*, vol. 2536, 1995, pp. 127-38.

118. Alfano, Robert R. "The Supercontinuum Laser Source." *The Supercontinuum Laser Source: The Ultimate White Light, ISBN 978-1-4939-3324-2. Springer Science+ Business Media New York*, 2016.

119. "Fizeau Interferometer for Optical Testing." LightTrans Gmbh 2021 https://www.lighttrans.com/use-cases/application-use-cases/fizeau-interferometer-for-optical-testing.html. Accessed July 24, 2021.

120. Granzow, Nicolai. "Supercontinuum White Light Lasers: A Review on Technology and Applications." *Joint TC1 - TC2 International Symposium on Photonics and Education in Measurement Science 2019*, vol. 11144, SPIE, 2019. https://doi.org/10.1117/12.2533094.

121. Singh, Manisha et al. "Beam Shaping of Supercontinuum Pulses." *Optical Systems Design 2015: Optical Design and Engineering VI*, vol. 9626, 2015, p. 962633.

122. Herráez, Miguel Arevallilo et al. "Fast Two-Dimensional Phase-Unwrapping Algorithm Based on Sorting by Reliability Following a Noncontinuous Path." *Applied optics*, vol. 41, no. 35, 2002, pp. 7437-44.

123. Zhao, Zixin et al. "Robust 2d Phase Unwrapping Algorithm Based on the Transport of Intensity Equation." *Measurement Science and Technology*, vol. 30, no. 1, 2018, p. 015201.

124. Gray, Robert. "Zernikecalc." 2021. https://www.mathworks.com/matlabcentral/fileexchange/33330-zernikecalc.

125. Lakshminarayanan, Vasudevan and Andre Fleck. "Zernike Polynomials: A Guide." *Journal of Modern Optics*, vol. 58, no. 18, 2011, p. 1678, doi:10.1080/09500340.2011.633763.

CHAPTER 3: REDUCTION OF RETRACE ERROR FROM BROADBAND VARIABLE TRANSMISSION SPHERES IN FIZEAU INTERFEROMETRY [126]

3.1 Introduction

3.1.1 Broadband Variable Transmission Spheres

We have previously reported on the use of Broadband Variable Transmission Spheres as potential alternatives to conventional transmission spheres [127, 128]. In Fizeau interferometry, transmission spheres transform incident wavefronts into high-quality spherical wavefronts to match the shapes of nominally spherical test surfaces for non-contact surface characterization [21, 71, 105-110, 128]. In this approach, a transmission sphere with appropriate f-number must be chosen such that the center of curvature of the surface under test and the focal plane of the transmission sphere are aligned, so that the curvature of the test wavefront matches the curvature of the test surface [119, 129, 130]. Traditional transmission spheres are designed for specific f-numbers and source wavelengths which limits the ranges of surface curvatures that an individual transmission sphere can measure. BVTS systems leverage the concept of Alvarez lenses to create a variable f-number transmission sphere functioning for a broad range of source wavelengths. BVTS systems have the potential to reduce the need for multiple transmission spheres, reduce the time needed for changing and calibrating transmission spheres to test different surface curvatures, and to increase the range of surface curvatures measurable with a single system. In Ref. [127], we investigated two BVTS designs and simulated surface measurements using these BVTS systems and concluded that they faced limitations in surface measurement accuracy due to residual system aberrations. In this paper we explore the nature of retrace errors and their significance in BVTS system performance limitations. We also present an optimization method to reduce retrace errors

in BVTS systems and present results for several examples that show significant reductions in retrace errors.

3.1.2 Retrace Error

In Fizeau interferometry it is assumed that light reflected from the reference and test surfaces, respectively, follow the same optical path back through the optical elements of the system, especially the transmission sphere [131-133]. This assumption requires that the test surface shape be perfectly matched to the incident wavefront shape; retrace error results when this assumption is not met. The simplest example of retrace error, ignoring additional surfaces or material impurities, is illustrated in Fig. 3.1. In Fig. 3.1(a) the rays enter an ideal system from the left to the reference and test surfaces and retrace back through the transmission sphere along the same path. In contrast, rays in Fig. 3.1(b) deviate before or at the test surface. Accordingly, the rays incident on the reference surface retrace through the system along the same path but the rays incident on the test surface do not, resulting in a path difference which we identify as retrace error. It is beneficial to separate retrace error into two types: alignment errors and transmitted wavefront errors. For spherical transmission spheres the primary measurement errors due to misalignment with the test surface are defocus and coma [131]. Similarly, aberrations in the transmitted wavefronts will result in retrace error corresponding to the imperfect spherical wave incident on the test surface. For spherical transmission spheres, transmitted wavefront errors are primarily due to surface deviations and machining errors or material impurities [131].
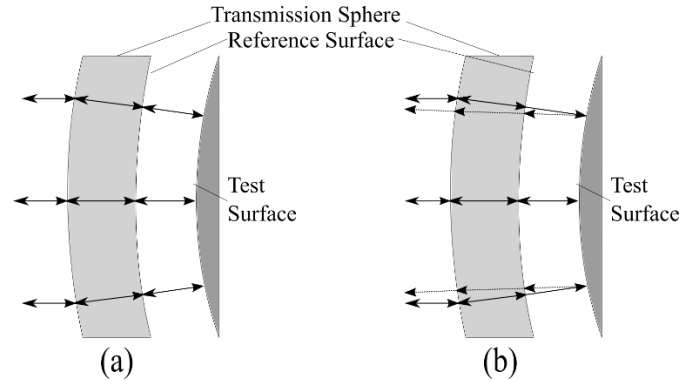
Fig. 3.1: Ray trace of interferometer (a) without, and (b) with retrace error

In our earlier work we noted the presence of significant aberrations in simulated surface measurements using BVTS [127]. In our idealized simulation, the test surfaces were not aberrated and alignment was not a contributing factor. This suggests that the aberrations present in the simulations are caused by retrace errors resulting from transmitted wavefront errors from the BVTS systems themselves.

3.2 Initial Designs and Simulation Methods

3.2.1 Initial BVTS System Designs

We previously presented two example BVTS system designs using Zemax OpticStudio™ [127]. Zygo's Transmission Sphere Selection Guide provided a guideline for systems with 101.6 mm entrance pupil diameter (EPD) [105]. F-numbers of the BVTS systems range from ± f/15 to ± f/80. Source wavelengths were chosen from visible to long-wave infrared laser wavelengths (0.6328 μm, 1.55 μm, 3.39 μm, and 10.6 μm). These BVTS systems used Zinc sulfide (ZnS) as the optical material because of its transmissivity and relatively low dispersion over the entire band of interest, but this concept can also be applied to other materials depending on manufacturability and transmissivity.

We now briefly summarize the designs and outcomes of these systems from Ref. [127]. In the first system, we added selected low-order polynomials to the basic Alvarez freeform surface and optimized the surface coefficients across the full range of f-numbers and design wavelengths with optimization targets of less than $\lambda/10$ peak to valley (PV) wavefront error (centroid) and diffraction limited spot sizes. A second system was also designed using techniques developed by Grewe et al. [56, 58]; additional polynomial terms were added to the freeform surfaces to address wavefront aberrations and the system was optimized using the same approach as the first system. Both example BVTS systems had diffraction-limited spot sizes and PV wavefront error of less than $\lambda/10$ for the IR source wavelengths. However, as discussed above, neither BVTS system resulted in the desired performance in the simulated measurements of test surfaces, showing that optimization metrics beyond spot size and PV wavefront error are required.

3.2.2 Fizeau Interferometer Simulation

A model for a 101.6 mm EPD Fizeau interferometer was built in VirtualLab Fusion™ to simulate our BVTS systems, as illustrated in Figure 3.2 [105]. Collimated sources were used with an aperture added after the BVTS to block unwanted light from interacting with the edges of the BVTS when configured to the maximum lateral shift. Light reflected from the reference and test surfaces were reflected to the detector by the beamsplitter, and the resulting interferogram was used for analysis.
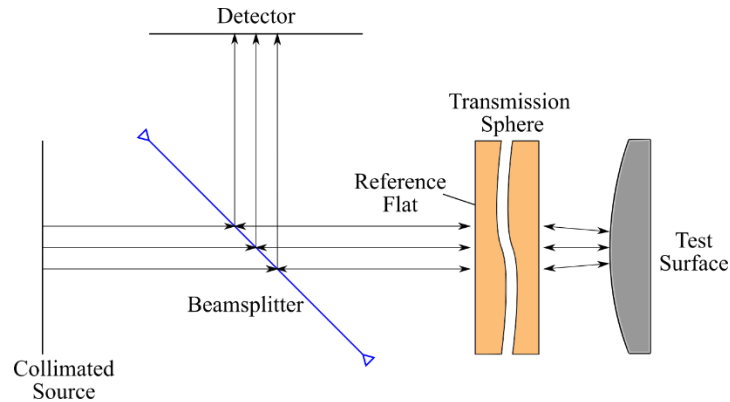
Fig. 3.2: Diagram view of Fizeau interferometer in VirtualLab Fusion™ for a convex surface.

To isolate the retrace error for the BVTS transmission sphere in the interferometer, only reflections from the reference surface and the test surface were considered; no reflections from intermediate surfaces of the BVTS system contributed to the interferogram, thereby ensuring that only transmitted wavefront retrace error is present in our simulated surface measurements. Alignment retrace error is not present because the simulated components were simulated with perfect alignment. All components except for the transmission sphere and test surface were 'ideal' components as defined in VirtualLab Fusion, limiting them to basic optical functions rather than objects with simulated material properties. For example, the 'ideal' beamsplitter is not a cube or plate beamsplitter but rather a simple field re-direction function. The reference and test wavefronts interfere with each other at the detector, resulting in an interferogram corresponding to variations in the test wavefront with respect to the reference wavefront. The corresponding BVTS configuration was simulated for each ideal wavefront and phase data from each resulting interferogram was exported as an ASCII file for analysis.

A MATLAB® script was written to import and evaluate phase data from the simulated interferograms obtained in VirtualLab Fusion™ using two algorithms to ensure proper phase unwrapping [122, 123]. Because the surface parameters are known in simulation, the ideal interferogram and the deviation in the surface measurement from the wavefront shape can be

calculated. Calculating the difference between the simulated and ideal surface maps provides a surface measurement height map of retrace errors induced by the BVTS transmission sphere; ideally, the resulting height map would be zero everywhere. Surface measurement PV and root mean square (RMS) magnitudes were calculated and the ZernikeCalc MATLAB® function was used to fit Fringe Zernike polynomials to the retrace-error map for aberration analysis [124].

3.3 Retrace Error Methods and Results

3.3.1 Retrace Errors of BVTS Examples 1 and 2

We previously reported on surface measurement data for BVTS Examples 1 and 2 obtained from the simulated Fizeau interferometer, as described in Section 2.2. The PV errors of surface measurements reported for BVTS Examples 1 and 2 (in Tables 2.6 through 2.8) were filtered by removal of the first four Fringe Zernike terms, a common practice for surface measurements. However, evaluation of the total retrace error requires inclusion of all the terms. To this end, we analyzed simulated wavefront data for test surfaces chosen to match a range of commercially available transmission spheres [105]. Specifically, r-numbers (test surface radius of curvature divided by test area diameter) from -81.5 to 80 were evaluated for 100-mm-diameter test surfaces. The resulting PV retrace errors are presented in Table 3.1.

Table 3.1: PV Retrace Errors for BVTS Examples 1 and 2

BVTS Example 1					BVTS Example 2				
	Source Wavelength (μm)					Source Wavelength (μm)			
	0.6328	1.55	3.39	10.6		0.6328	1.55	3.39	10.6
r-number	PV (waves)				**r-number**	PV (waves)			
80	0.72	0.50	0.20	0.04	**80**	1.25	0.56	0.15	0.05
45	0.61	0.53	0.10	0.10	**45**	2.16	1.03	0.46	0.08
35	0.67	0.56	0.13	0.04	**35**	2.94	1.48	0.53	0.10
25	1.21	0.55	0.32	0.05	**25**	3.37	1.56	0.75	0.14
15	1.76	0.82	0.38	0.06	**15**	6.06	2.62	1.35	0.35
-81.5	1.16	0.76	0.09	0.02	**-81.5**	1.19	0.55	0.14	0.05
-46	1.23	0.56	0.32	0.04	**-46**	2.12	1.01	0.28	0.08
-36	1.25	0.63	0.17	0.06	**-36**	2.67	1.15	0.51	0.11
-26	1.98	1.00	0.39	0.08	**-26**	4.03	2.01	0.63	0.16
-16	2.28	1.03	0.48	0.25	**-16**	6.03	2.59	1.35	0.31

Since the first four Fringe Zernike terms are not removed in the retrace error evaluation, the magnitudes of the PV retrace errors are higher than the PV surface measurement errors previously reported [127]. From this, only the LWIR systems in either of these two BVTS cases can be expected to perform with less than $\lambda/10$ PV retrace error. This does not preclude the other source wavelengths from potential use, but drastically limits their expected performance in these BVTS systems. For these reasons, it is important to identify the primary contributors to retrace error as well as to determine if there is the potential to address them.

The largest differences between the two initial BVTS systems were in x-tilt, y-tilt, oblique astigmatism, and vertical coma, as demonstrated in Tables 2.7 and 2.8. If we compare tilt terms between the systems, it is obvious that BVTS Example 1 possesses unwanted aberrations in both tilt terms while BVTS Example 2 has a negligible y-tilt with a significantly larger x-tilt. While the combination of x- and y-tilts is undesired, the overall magnitude is less in the first system. For the second system, x-tilt terms and fringes across the source wavelengths proved challenging for the phase unwrapping procedure, which dominated the PV retrace error as can be seen comparing

results from Table 3.1 above and Table 2.5. The tilt terms present must be due to transmitted wavefront error, implying the freeform surfaces are introducing a tilt term to the wavefront and exacerbating it upon the second pass through the BVTS.

As to why these aberrations arise, the analytical design approach behind the Alvarez lens concept (and therefore the BVTS systems) assumes the freeform surfaces are in the same plane [56]. However, there must be some space between the freeform surfaces to avoid collisions. As a consequence, the wavefront modified by the first freeform surface has propagated some distance to the second freeform surface and therefore is deviated from an ideal shape [56]. While symmetry breaking of the freeform surfaces can be used to reduce aberrations for imaging systems, surface symmetry is more desirable in the current case where the test wavefront returns through the BVTS.

3.3.2 Optimization Method for Reduced Retrace Error: BVTS Example 3

To reduce retrace error, optimization metrics must consider the wavefront aberrations generated by the freeform surfaces in the BVTS [51-53, 56]. Optimizing the freeform surfaces with the target of uniform interferograms (corresponding to ideal measurements of ideal surfaces) from the simulated Fizeau system for the full measurement range of the BVTS is computationally challenging. Instead, we optimize the BVTS system across the full range as an imaging system to minimize PV wavefront error and to reduce the aberrations with the highest contribution in the focal plane; reducing transmitted wavefront error should reduce retrace error [131]. From the Zemax OpticStudio™ User Manual, wavefront error with respect to centroid is calculated by removing piston and tilt [134]. Since tilt terms were present in our previous results, the optimization should target minimized PV wavefront error referenced to the chief ray instead, which does not remove the tilt terms.

For a new optimized design addressing the measurement aberrations of the initial systems, we started from the BVTS Example 2 system and created a merit function in Zemax OpticStudio™ to minimize PV wavefront error (chief ray) and specific Fringe Zernike polynomial wavefront aberrations in the image plane. The Fringe Zernike terms with the highest variation across all configurations for the BVTS Example 2 system were assigned targets of 0 and equal weighting for 40 configurations in the multi-configuration editor (10 different f-numbers each for four wavelengths). The terms with the highest initial contribution were piston (Z1), x-tilt (Z2), defocus (Z4), horizontal coma (Z7), spherical (Z9), horizontal trefoil (Z10), secondary horizontal coma, (Z14), horizontal tetrafoil (Z17), secondary horizontal trefoil (Z19), and horizontal pentafoil (Z26). We previously reported that significant contributions from x-tilt, defocus, horizontal coma, and spherical were present in the surface measurement aberrations for this system (Table 2.8). Therefore, by optimizing the surface coefficients to minimize the image plane wavefront aberrations, we intend to reduce the surface measurement aberrations accordingly.

The original 4th order polynomial system of BVTS Example 2 showed improvement up to the Z9 (Spherical) aberration term after optimization. Since higher order surface polynomials were needed to address higher order aberrations, we used a more general form for the freeform surfaces for the new BVTS design:

$$z(x, y) = \sum a_{m,n} x^m y^n \tag{3.1}$$

Using the surface form of Equation 3.1, we incremented one order (defined by the sum of m and n in Equation 3.1) at a time, optimizing with each iteration. The merit function had diminishing improvements (on the order of 10^{-5}) as 10th order surface polynomials were added. While optimizing, it was observed that the y term offered no advantage and the x^2 term contributed a significant amount of x-tilt (Z2) aberration regardless of optimization. The surface coefficients for

the resulting example BVTS design are shown in Table A.1 of Appendix A, and the resulting PV wavefront error (chief ray) in the focal plane is shown in Table 3.2.

The PV wavefront error (chief ray) in the focal plane did not significantly improve (and in some configurations slightly worsened) when compared to corresponding results for BVTS Examples 1 and 2 (presented in Tables 2.3 and 2.5). This strongly suggests, again, that diffraction limited spot size and the total PV wavefront error of the BVTS systems in the focal plane are not the best optimization metrics for the BVTS systems. However, as will be discussed below, the retrace error was significantly reduced for the third system compared to the initial systems, likely due to reduction in magnitude of the selected Fringe Zernike wavefront aberration terms.

Table 3.2: PV Wavefront Errors (chief ray) for BVTS Example 3

	Source Wavelength (µm)			
	0.6328	1.55	3.39	10.6
f-number	PV (waves)			
f/15	0.824	0.361	0.170	0.063
f/25	0.523	0.195	0.089	0.029
f/35	0.558	0.187	0.084	0.026
f/45	0.572	0.197	0.087	0.025
f/80	0.592	0.209	0.093	0.026

3.3.3 Retrace Errors of BVTS Example 3

As just discussed, BVTS Example 3 was optimized with the goal of reduced retrace errors. We simulated the use of this new design for the same ideal surfaces as BVTS Examples 1 and 2. The resulting PV retrace errors for BVTS Example 3 are presented in Table 3.3.

Table 3.3: PV Retrace Errors for Ideal Surface Measurements

	BVTS Example 3			
	Source Wavelength (µm)			
	0.6328	1.55	3.39	10.6
r-number	**PV (waves)**			
80	0.53	0.19	0.05	0.03
45	0.63	0.41	0.06	0.02
35	0.66	0.38	0.23	0.06
25	0.83	0.35	0.11	0.03
15	1.36	0.50	0.34	0.04
-81.5	0.59	0.21	0.08	0.04
-46	0.86	0.37	0.11	0.03
-36	0.73	0.40	0.22	0.03
-26	1.02	0.43	0.13	0.04
-16	1.37	0.64	0.17	0.07

3.4 Discussion

The PV retrace errors for BVTS Example 3 are drastically reduced for the shorter source wavelengths in comparison to the PV retrace errors reported in Table 3.1 for the two initial designs,. These errors also remain below $\lambda/10$ for the 10.6 µm and much of 3.39 µm, which was not achieved in either of the previous BVTS system examples. While perhaps still insufficient for precise surface measurements, across the full ranges tested, the PV error for BVTS Example 3 is less than $\lambda/2$ for all IR source wavelengths (except the r/16 concave configuration for 1.55 µm) and less than λ for the visible source wavelength, indicating significantly improved performance over the previous systems. To visually illustrate this improvement, Figure 3.3 compares representative results of wrapped interferogram phase for the three BVTS systems for a range of r-numbers. Constant phase across the interferogram corresponds to zero retrace error (no path difference for an ideal surface). Notably, x-tilt is visibly present in BVTS Example 2, and the phase is much more constant for BVTS Example 3. The improved PV error metric of the retrace error maps and the more constant phase for BVTS Example 3 indicate that our optimization method is

successful in reducing retrace error. It is feasible that further reductions may be possible with refined optimization procedures.
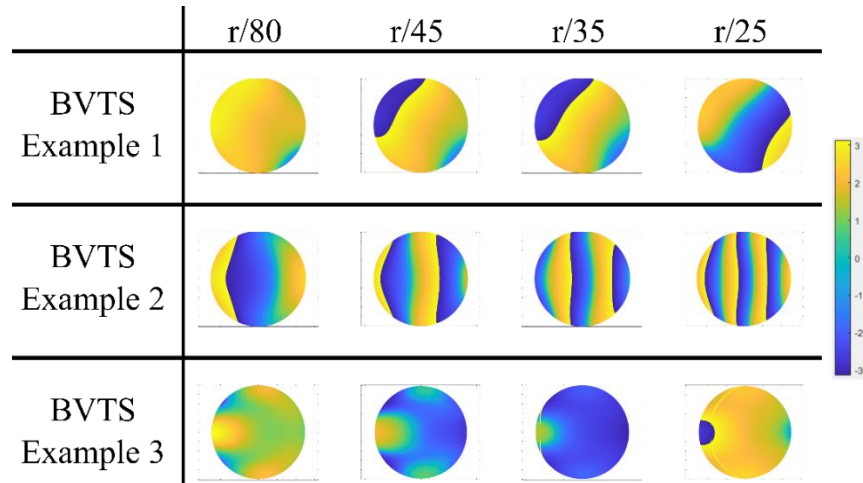
Fig. 3.3: Interferogram phase (radians from $-\pi$ to $+\pi$) for 1.55 μm source with each BVTS Example for convex surfaces, 100 mm diameter.
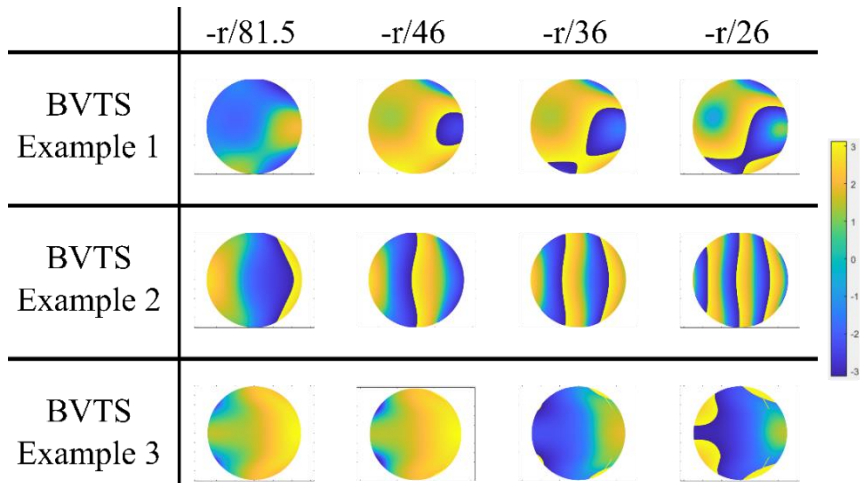
Fig. 3.4: Interferogram phase (radians from $-\pi$ to $+\pi$) for 1.55 μm source with each BVTS Example for concave surfaces, 100 mm diameter.

While wrapped phase is useful for visually demonstrating the aberration effects, unwrapped phase is used to determine the height maps and is more conducive to quantification of the constancy of the interferogram and surface measurements. To this end, the root-mean-square (RMS) error of the unwrapped interferogram phase maps was calculated for each case to provide

a quantitative metric for comparison. RMS is useful for determining the variation of values with respect to the arithmetic mean; a smaller RMS value corresponds to a greater degree of constancy. RMS values and the standard deviation σ of the RMS values for the unwrapped interferograms are reported in Table 3.4. As can be seen, the non-symmetrical aberrations of Example 1 introduce a degree of inconsistency and the tilt terms in Example 2 introduce significant deviation for the faster r-numbers. Example 3 demonstrates a significant improvement over the initial two systems, along with a more consistent performance across the range of positive and negative r-number surfaces.

Table 3.4: RMS of Example Unwrapped Interferogram Phase Profiles

	r-number								
	80	45	35	25	-26	-36	-46	-81.5	
BVTS	RMS (mrad)								σ (mrad)
Example 1	6.1	8.3	14.8	2.9	6.7	8.3	7.6	6.1	3.2
Example 2	7.3	23.6	53.3	6.4	80.0	23.6	14.5	7.3	23.6
Example 3	4.8	5.2	8.0	7.2	6.0	5.2	1.8	4.8	1.7

3.5 Conclusions

We have demonstrated that BVTS systems can replace several conventional transmission spheres with one Alvarez lens-based system, but that the systems can fall short of target performance (except in the LWIR) due to retrace error. We have demonstrated an improved optimization method targeting specific wavefront aberrations to significantly reduce retrace error. The improved BVTS system brings the shorter source wavelengths closer to viability for surface measurements. It is likely that the initial BVTS systems are ambitious in their source wavelength range; reduced ranges and changes in optical materials may result in further improvements for shorter source wavelengths when coupled with updated optimization metrics. Future work to develop optimization methods for the design of BVTS systems related directly to constant interferogram phase along with the demonstrated transmitted wavefront aberration optimization may further enable improved surface measurements.

3.6 Appendix A

Table 3.5: Surface Coefficients for BVTS Example 3

Polynomial Orders (x^m, y^n)		Coefficient a_{mn} mm^{1-m-n}	Polynomial Orders (x^m, y^n)		Coefficient a_{mn} mm^{1-m-n}	Polynomial Orders (x^m, y^n)		Coefficient a_{mn} mm^{1-m-n}
m	n		m	n		m	n	
1	0	-1.16E-02	3	3	-4.69E-18	9	0	-2.19E-22
1	1	6.34E-09	2	4	1.67E-14	8	1	5.46E-25
0	2	-1.04E-04	1	5	3.09E-16	7	2	-3.31E-21
3	0	1.04E-06	0	6	5.36E-11	6	3	8.93E-24
2	1	-1.29E-12	7	0	-6.20E-19	5	4	1.42E-20
1	2	3.12E-06	6	1	-1.53E-20	4	5	3.02E-23
0	3	-8.25E-09	5	2	-4.44E-17	3	6	-1.07E-19
4	0	6.25E-12	4	3	-1.64E-19	2	7	1.12E-22
3	1	-1.86E-15	3	4	2.38E-16	1	8	1.11E-19
2	2	8.19E-12	2	5	-6.91E-19	0	9	4.94E-19
1	3	-2.20E-13	1	6	-6.26E-16	10	0	-2.55E-24
0	4	-3.06E-08	0	7	-3.47E-15	9	1	3.84E-26
5	0	3.85E-14	8	0	6.31E-20	8	2	-5.92E-23
4	1	1.81E-16	7	1	-6.58E-22	7	3	-3.59E-26
3	2	-8.77E-16	6	2	7.83E-19	6	4	-8.96E-23
2	3	1.51E-15	5	3	5.61E-22	5	5	1.48E-25
1	4	1.54E-12	4	4	7.09E-20	4	6	1.97E-23
0	5	8.46E-12	3	5	-7.70E-22	3	7	1.35E-25
6	0	-5.39E-16	2	6	-6.01E-18	2	8	7.76E-22
5	1	3.29E-18	1	7	-1.61E-19	1	9	2.80E-23
4	2	-1.75E-15	0	8	-2.05E-14	0	10	2.63E-18

REFERENCE LIST

21.   Wang, Yan et al. "Design of Multi-Wavelength Achromatic Transmission Sphere Based on Zoom Principle." *Proc. SPIE*, *Optical Metrology and Inspection for Industrial Applications VII*, vol. 11552, 2020, p. 1155217.

51.   Alvarez, Luis W. "Two-element variable-power spherical lens." U.S. Patent No. 3,305,294. 21 Feb. 1967.

52.   Babington, James. "Alvarez Lens Systems: Theory and Applications." *Proc. SPIE, Optical Systems Design 2015: Optical Design and Engineering VI*, vol. 9626, 2015, p. 962615.

53.   Barbero, Sergio. "The Alvarez and Lohmann Refractive Lenses Revisited." *Optics express*, vol. 17, no. 11, 2009, pp. 9376-90.

56.   Grewe, Adrian et al. "Aberration Analysis of Optimized Alvarez–Lohmann Lenses." *Applied optics*, vol. 53, no. 31, 2014, pp. 7498-506.

58.   Smilie, Paul J et al. "Design and Characterization of an Infrared Alvarez Lens." *Optical Engineering*, vol. 51, no. 1, 2012, p. 013006.

71.   Peng, Wei-Jei et al. "Design, Tolerance Analysis, Fabrication, and Testing of a 6-In. Dual-Wavelength Transmission Sphere for a Fizeau Interferometer." *Optical Engineering*, vol. 56, no. 3, 2017, p. 035105.

105.   "Zygo Transmission Sphere Selection Guide." edited by ZYGO, 2014, 4. https://bit.ly/2ZNMqbK.

106.   Yang, Pengqian et al. "Transmission Sphere Calibration and Its Current Limits." *Proc. SPIE, Optical Measurement Systems for Industrial Inspection VII*, vol. 8082, 2011, p. 80822L.

107.   Gao, Zhishan et al. "Computer-Aided Alignment for a Reference Transmission Sphere of an Interferometer." *Optical Engineering*, vol. 43, no. 1, 2004, pp. 69-74.

108.   Peng, Wei-Jei et al. "Design and Tolerance Analysis of a Transmission Sphere by Interferometer Model." *Proc. SPIE, Optical System Alignment, Tolerancing, and Verification IX*, vol. 9582, 2015, p. 958208.

109.   Peng, Wei-Jei et al. "Mounting of Reference Surface for a Transmission Sphere." *Proc. SPIE, 8th International Symposium on Advanced Optical Manufacturing and Testing Technologies: Optical Test, Measurement Technology, and Equipment*, vol. 9684, 2016, p. 96840G.

110.   Pinto, Joseph. "Transmission Spheres More Than Just a Reference Surface!" *Optifab 2003: Technical Digest*, vol. 10314, 2003, p. 1031415.

119.   "Fizeau Interferometer for Optical Testing." LightTrans Gmbh 2021 https://www.lighttrans.com/use-cases/application-use-cases/fizeau-interferometer-for-optical-testing.html. Accessed July 24, 2021.

122.   Herráez, Miguel Arevallilo et al. "Fast Two-Dimensional Phase-Unwrapping Algorithm Based on Sorting by Reliability Following a Noncontinuous Path." *Applied optics*, vol. 41, no. 35, 2002, pp. 7437-44.

123.   Zhao, Zixin et al. "Robust 2d Phase Unwrapping Algorithm Based on the Transport of Intensity Equation." *Measurement Science and Technology*, vol. 30, no. 1, 2018, p. 015201.

124.   Gray, Robert. "Zernikecalc." 2021. https://www.mathworks.com/matlabcentral/fileexchange/33330-zernikecalc.

126.   Koerber, Jonathan et al. "Reduction of Retrace Error from Broadband Variable Transmission Spheres in Fizeau Interferometry." *Optics Continuum*, 2022, doi:https://doi.org/10.1364/OPTCON.458860.

127.   Koerber, Jonathan et al. "Broadband Variable Transmission Sphere for Fizeau Interferometry." *Optics*, vol. 3, no. 1, 2022, pp. 88-98, https://www.mdpi.com/2673-3269/3/1/11.

128.   Koerber, Jonathan and Thomas J Suleski. "Design of a Broadband Variable Transmission Sphere." *Frontiers in Optics*, Optical Society of America, 2020, p. FM1A. 7.

129.   He, Yiwei et al. "Modeling Fizeau Interferometer Based on Ray Tracing with Zemax." *Proc. SPIE, AOPC 2015: Optical Test, Measurement, and Equipment*, vol. 9677, 2015, p. 96770G.

130.   Huang, Chunsheng. "Propagation Errors in Precision Fizeau Interferometry." *Applied optics*, vol. 32, no. 34, 1993, pp. 7016-21, doi:10.1364/AO.32.007016.

131.   Kreischer, Cody B. "Retrace Error: Interferometry's Dark Little Secret." *Proc. SPIE, Optifab 2013*, vol. 8884, 2013, p. 88840X.

132.   Geary, Joseph et al. "Retrace Error: A Case Study." *Proc. SPIE, San Diego 1992*, vol. 1776, 1992, https://doi.org/10.1117/12.139232.

133.   Han, Sen and Erik Novak. "Retrace Error for the Measurement of a Long-Radius Optic." *Proc. SPIE, ICO XVIII 18th Congress of the International Commission for Optics*, vol. 3749, 1999, https://doi.org/10.1117/12.354906.

134.   "User Manual." *Zemax OpticStudio 22.1*, 2022, p. 1091.

CHAPTER 4: BROADBAND BEAM SHAPING WITH TRANSMISSIVE FREEFORM OPTICS

4.1 Introduction

4.1.1 Beam Shaping

Beam shaping is the process of redistributing the irradiance and phase of a beam of light from an input distribution to a different output distribution [80]. Beam shaping has existed throughout history from records of Greeks designing burning glasses to 19th century Fresnel lenses in lighthouses [80]. Today a significant use of beam shaping is the conversion of a laser beam's Gaussian irradiance distribution to a beam profile that is uniform over at least one cross-section (see Figure 4.1) [78, 80, 81, 135]. Applications of laser beam shaping include lithography, material processing, data storage, metrology, material characterization, biomedical sensing, EO/IR, and more [80]. Due to the narrow spectral bandwidth of most laser sources, commercially available laser beam shapers and laser beam shapers in the literature are primarily monochromatic [33, 44, 60, 61, 80, 81, 86-90, 92, 96, 136-143]. Achromatic laser beam shapers exist and are useful for a variety of source bandwidths thus enabling reduction of the number of optical components kept in a lab for any application requiring multiple source wavelengths [15, 20, 28-30, 43, 118, 121]. For example: commercial supercontinuum lasers, which mostly extend from 0.4 to 2.4 µm in wavelength, have applications in biomedical optics, confocal microscopy, fluorescence lifetime imaging microscopy, optical coherence tomography, and flow cytometry [118, 120, 121]. Controlled irradiance distribution over a given area for multiple wavelengths is helpful in these applications and others where similarity in incident area of the different wavelengths (effectively achromatic performance) is desired for consistent characterization of sample surfaces or areas under test [120].
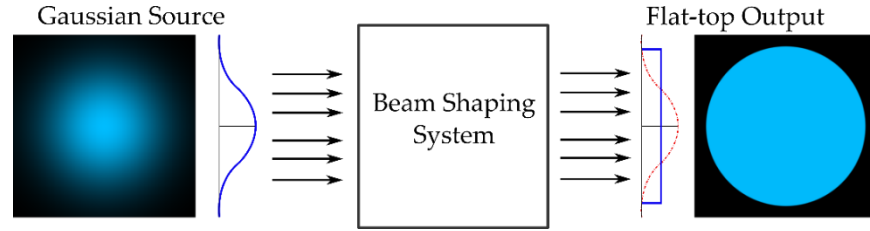
Fig. 4.1: Illustration of Gaussian to flat-top laser beam shaping
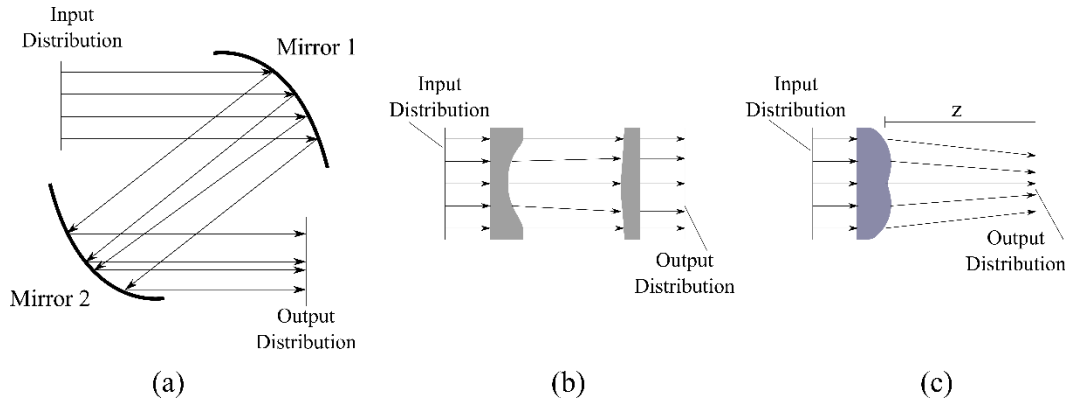
Fig. 4.2: General Configurations of (a) Reflective and (b) Afocal and (c) Focal Transmissive Beam Shapers

Reflective, transmissive, and diffractive laser beam shapers have been presented in the literature or are available commercially with most using off-axis parabolas [69], mild aspheric surfaces [81, 88, 89, 137, 138], or structured optical surfaces [9, 20, 82, 97] respectively to achieve the desired irradiance redistribution. In this paper, we focus on the more commonly available transmissive beam shapers. Afocal transmissive laser beam shapers require at least two optical elements and are commercially available [30, 137, 139, 140]. Afocal transmissive beam shapers either redistribute the beam while maintaining the spot diameter or changing the output dimensions with respect to the input dimensions [28, 137, 142, 144]. Commercially available achromatic beam shapers are afocal and use two aspheric surfaces for beam shaping and add at least one spherical optical element for chromatic aberration correction [29, 30]. In either case, afocal systems have separation between the surfaces used to redistribute the beam due to collimation constraints based on telescope geometries [28, 29, 80, 136, 137]. As a consequence of the ray mapping method, it is

possible to achieve broadband performance with an afocal beam shaper without achromatic performance. By changing the distance between the beam shaping surfaces the system can function for different wavelengths than the design wavelength as long as the optical materials are transmissive [44]. Equation 4.1 relates the separation-dependent broadband relationship of an afocal beam shaper as illustrated in Figure 4.3.

$$d_2 = d_1 \frac{n(\lambda_1) - 1}{n(\lambda_2) - 1} \tag{4.1}$$
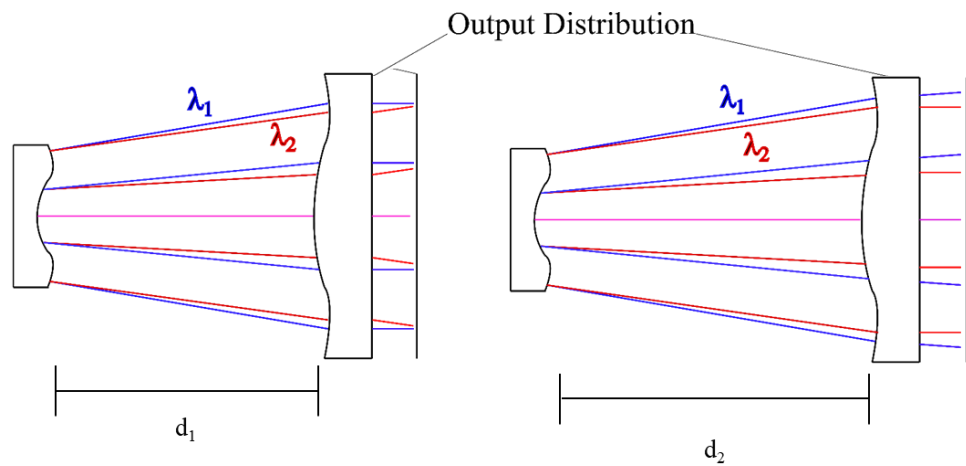
Fig. 4.3: Afocal Beam Shaper Broadband by Separation Dependence Illustration

Focal transmissive beam shapers are also available in two forms, either as a combination of a focusing lens following an afocal beam shaper or as a single optical element with a surface determined by a ray mapping solution [44, 81, 84, 86, 135]. Commercial methods for uniform non-radial output distributions from transmissive beam shapers rely on birefringent materials or additional optical elements after the beam shaping system such as an aperture mask or cylindrical lens, which results in a loss of energy [88]. In this paper, we will focus on achromatic and broadband transmissive beam shapers with freeform surfaces, with the goal of achieving non-radial uniform output profiles without requiring birefringent materials, additional optical elements, or masking of the output irradiance distribution.

4.1.2 Freeform Beam Shaping

Freeform optics, defined as optics which have at least one surface lacking in translational or rotational symmetry, enable unique output distributions. Since freeform surfaces are not constrained to the radial symmetry of aspheres used for conventional transmissive beam shapers, they have the ability to convert radially symmetric inputs such as Gaussian beams to non-radially symmetric outputs without the use of additional cylindrical optics or masking elements [60, 88]. Freeform beam shapers with non-radially symmetric outputs follow the ray-mapping design processes of radial output systems but change the ray mapping equations by solving for optimal mass transport using Monge-Ampère equations or, as is presented here, by changing the integral for conservation-of-energy constraints [59, 62, 145]. In this paper we investigate several methods of applying achromatic design methods to freeform beam shapers. We first combine afocal beam shaping designs with spherical optical elements of a different material for chromatic aberration correction using conventional methods with a different approach to ray mapping to achieve a square output distribution. Second, we combine the design concepts of an achromatic doublet to focal beam shapers with a similar ray mapping approach to achieve a square output distribution at a fixed distance using both spherical and freeform surfaces.

4.2 Beam Shaper Design Methods

4.2.1 Non-Radial Output Beam Shaper Design

The design of beam shapers relies on the principle of energy conservation [79, 146, 147]. The primary condition to be satisfied for energy conservation in polar coordinates is:

$$\int_0^{2\pi}\int_0^{r_o} I_1(r)rdrd\theta = \int_0^{2\pi}\int_0^{R_o} I_2(R)RdRd\theta \tag{4.2}$$

Simply stated, the energy conservation requirement is that the integral of the irradiance of the input beam (I_1) with respect to the input coordinates (r) or (x,y) must be equal to the integral of the irradiance of the output beam (I_2) with respect to the output coordinates (R) or (X,Y). The above integral can be rewritten in Cartesian coordinates as needed for non-radially symmetric beams [100]. Equation 4.3 shows the alternative form of the energy conservation integrals.

$$\iint I_1(x,y)dxdy = \iint I_2(X,Y)dXdY \tag{4.3}$$

For a given input dimension r_o or x_o and a target output dimension R_o or X_o, we can solve the integral relationships to develop a ray mapping function from the input distribution to the target output distribution [44, 137, 142-144, 148]. We can use the ray mapping function to solve integrals or differential equations, for afocal and focal systems respectively, relating the slope of the beam shaping surface to the refractive index of the material, input and output coordinates, and the separation between beam shaping surfaces for an afocal system, or the distance to the focal plane for a focal system [44, 100, 137, 144, 148]. The surface shape is then fitted to a polynomial equation to describe the full surface in simulation software. For the afocal systems here, aspheric polynomial coefficients are used. While for a radial distribution the surface coefficients are fit to radial equations, in the case of a non-radial output distribution we instead fit to coefficients in x and y cross-sections separately, resulting in the required non-radially symmetric surface description. For the designs presented below, the desired output distribution is a flat-top square area in which the uniformity of the freeform beam shaper output should resemble a step function in cross section [100]. For generating a square output distribution, the ray mapping equation is shown in Equation 4.4 where x is the coordinate reference of the input rays and X is the output coordinate, I_o is the constant irradiance of the output, ω_o is the beam waist radius, and *erf* is the error function [100].

$$X(x) = \frac{\omega_o}{I_o} \frac{\sqrt{2\pi}}{4} erf(\sqrt{2} \frac{x}{\omega_o})$$

(4.4)

For the design of an afocal freeform beam shaper, the inverse of the ray mapping function is used with the ray mapping function to determine the surface cross sections in x and y using the following integrals where *x(X)* is the inverse of the ray mapping function, *n* the index of refraction of the material, and *d* is the separation of the beam shaping surfaces [44]. In the case of the square output distribution used here the surface relationships are separable such that we can solve for x or y orientations individually with the same form shown in Equations 4.5 and 4.6 [100].

$$z(x) = \int_0^x \left\{ (n^2 - 1) + \left[\frac{(n-1)d}{X(x) - x} \right]^2 \right\}^{-\frac{1}{2}} dx$$

(4.5)

$$Z(X) = \int_0^X \left\{ (n^2 - 1) + \left[\frac{(n-1)d}{x(X) - X} \right]^2 \right\}^{-\frac{1}{2}} dX$$

(4.6)

4.2.2 Achromatic Method for Focal Beam Shaper

In a focal beam shaper, the focal beam shaping element is only one material and is designed for one index of refraction, thus we must introduce a second optical element of a different material to correct for chromatic aberration to achieve achromatic beam shaping [1]. We propose the use of spherical or freeform optical elements paired with a focal beam shaping element. The advantage of a nominally cemented achromatic focal beam shaper is the compactness of the system which would enable it to, for example, be paired with the endcap of a fiber laser.

Adding a lens of a given optical power after the freeform element will change the dimensions of the output spot size as well as the effective distance to the focal plane. It is therefore necessary to predict the change in output distribution dimensions to choose appropriate constraints for our

freeform surface design, which can be accomplished analytically by paraxial approximations. In analogy, this plano-freeform and spherical optical element pair would be designed using the constraints of an achromatic cemented doublet or those of an air-spaced achromat [1]. The primary advantage of this method over afocal methods is the compactness of the elements as they are nominally 'cemented' and therefore the overall system length will be roughly the overall thickness of the two elements rather than requiring air-spaced thicknesses. If we assume the usual achromatic doublet design constraints, we have Equation 4.7 [1].

$$\varphi_a + \varphi_b = \varphi \tag{4.7}$$

If we treat the target distance of the beam shaper's redistribution as the focal length of the beam shaper then the inverse of the target distance z_o is equal to φ_a the 'optical power' of the beam shaping element. φ_b is the optical power of the spherical lens, and φ is the total optical power. In the case of a Gaussian to a flat-top beam shaper, the regions are defined by the radii of the beam shaping lens (r_o) and the output target dimension (R) as seen in Figure 4.4. For the systems presented here we assume doublet constraints: the separation between the elements of the focal systems is nominally zero (some separation shown in Figure 4.4 for visual clarity).
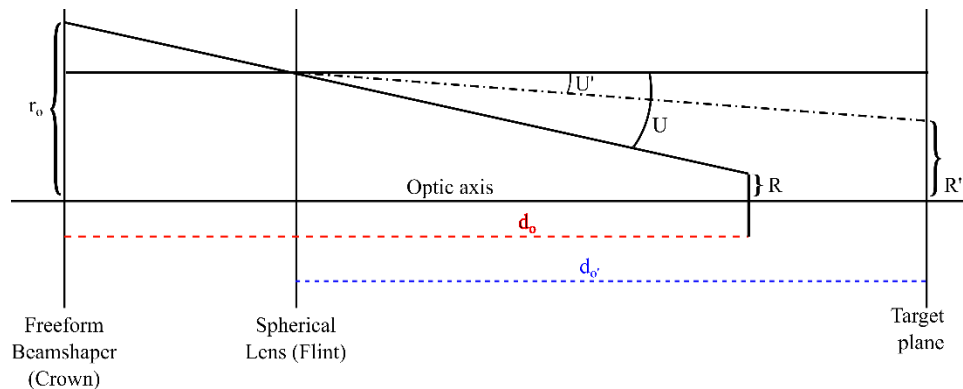
Fig. 4.4: Paraxial ray trace diagram of beamshaper and spherical lens achromatic pair

Therefore, the new output target dimension (R') due to the added spherical lens can be calculated analytically. For simplicity we use only R and R' in the development, which are

interchangeable with *X* and *X'* for a non-radial distribution. By determining the relationship between the focal beam shaping element's target output and the actual output of the achromatic pair we can adapt the focal beam shaping element's design to an appropriate output dimension to achieve the desired design performance. Our starting assumption is that that the redistributed rays are confined within the dimensions of the input and output parameters of the beam shaper, resulting in boundary rays at the edges of the beam whose path through the system can be handled with paraxial assumptions. From paraxial ray trace equations we have the following Equation 4.8 [1]:

$$u' = u - y\varphi \tag{4.8}$$

Here *u'* is the slope of the ray after the optical element ($\tan(U')$ in Figure 4.4), *u* is the slope of the ray incident on the optical element ($\tan(U)$ in Figure 4.4, exaggerated graphically for illustration purposes), *y* is the incident ray height, and φ_i is the optical power of the element. From the above constraints we have [1]:

$$y = r_o \tag{4.9}$$

$$u = \frac{R_o - r_o}{d_o} = (R_o - r_o)\varphi_a \tag{4.10}$$

$$u' = \frac{R' - r_o}{d_{o'}} = (R' - r_o)\varphi \tag{4.11}$$

Substituting Equations 4.9, 4.10, and 4.11 into Equation 4.8 we have:

$$(R' - r_o)\varphi = (R_o - r_o)\varphi_a - r_o\varphi_b \tag{4.12}$$

Expanding the terms and solving for *R'* we have:

$$R' = R_o \frac{\varphi_a}{\varphi} + r_o - r_o \frac{\varphi_a + \varphi_b}{\varphi} = R_o \frac{\varphi_a}{\varphi} \tag{4.13}$$

The optical powers of the first lens (in our case the beam shaper) and the total system optical power are related to each other by the Abbe numbers (υ_a and υ_b respectively with $\Delta\upsilon$ being the difference between υ_b and υ_a) of the materials being used [1]:

$$\varphi_a = \frac{\upsilon_a}{\Delta\upsilon}\varphi \tag{4.14}$$

We can see that Equation 4.13 becomes:

$$R_o = \frac{\varphi}{\varphi_a}R' = \frac{\Delta\upsilon}{\upsilon_a}R' \tag{4.15}$$

From this we can predict the scale of the magnified flat-top distribution of a nominally cemented doublet beam shaper in the target plane for a given target distance d_o or total system optical power φ. We then design our beam shaping element with a target output dimension and distance determined by Equation 4.15 with respect to the desired output radius and focal length when combined with the spherical optical element for achromatic correction. It should be noted that, due to the non-spherical shape of the beam shaping surface, we cannot have a truly cemented doublet as assumed here. In the case of a paired set of freeform surfaces for achromatic focal beam shaping, the optical power constraints are used to determine the parameters of both surfaces.

In order to find the surface profile of the focal beam shaper we use the following differential equation which relates the surface slope to the input and output parameters [58, 60, 61, 148]. This specific form of the equation for a square or rectangular beam shaping surface was derived and demonstrated by Shultz [100]. Here d_o is the distance to the focal plane and $z(x)$ is the beam shaping surface cross-section in x:

$$\frac{dz}{dx} = \frac{X - x}{(n-1)[d_o - z(x)]} \tag{4.16}$$

As a method of determining the reasonableness of a focal beam shaper design we use the dimensionless beam shaping parameter β [135].

$$\beta = \frac{CrR}{\lambda d} \tag{4.17}$$

β can be used to measure how well the geometrical-optic limit (a small-wavelength approximation) applies to a beam shaping element [135]. This term is related to the shape of the output by a shape related constant (C), the input and output dimensions (r and R), the source wavelength (λ), and the beam shaping element separation or focal length (d) of the beam shaping element as shown in Equation 4.17 [135]. Broadly speaking, for β values of ≥ 32 we should be able to use geometrical-optic designs to achieve adequate beam shaping. However, while a larger value of β corresponds to a shorter separation or focal length, ray mapping assumes near paraxial propagation of the beam which requires longer distances. Hence there is a balance to be sought wherein a suitably short separation or focal length is chosen to improve the quality of the output of a focal beam shaper without violating paraxial assumptions.

4.3 Simulation and Evaluation Methods

We designed several systems for different bands of source wavelengths based on available laser systems and beam shaping systems, and to demonstrate differences in material parameters and source wavelength spectra. We use two metrics for evaluating the redistribution performance. First is the dimension of the output spot standard deviation across source wavelengths. Second is the plateau uniformity (U_P) of the output spot in keeping with ISO 13694 [149, 150]. U_P is determined by taking a histogram of the energy across the output area, calculating the full-width at half-maximum (FWHM) of the histogram, and dividing the FWHM by the maximum energy of the output spot. A uniform spot results in a histogram with a sharp peak slightly below or at the

maximum energy. For an ideal uniform spot we expect a small FWHM and a U_P value approaching 0, whereas for a system dominated by a Gaussian profile or noise we expect a value approaching 1. Thus, U_P can be reported as a unitless value or a percentage [150]. An advantage of the U_P parameter lies in its shape independence for radially and non-radially symmetric output distributions. U_P is reported in our results as an average across source wavelength results as there will be slight variation due to wavelength dependent beam divergence. Output energy distributions shown are normalized to the maximum energy density value in the distribution. In order to help visualize the relationship between the U_P term and the quality of the output, Figure 4.5 demonstrates three instances of output distributions with their respective cross-sections and histograms used to determine the U_P term.
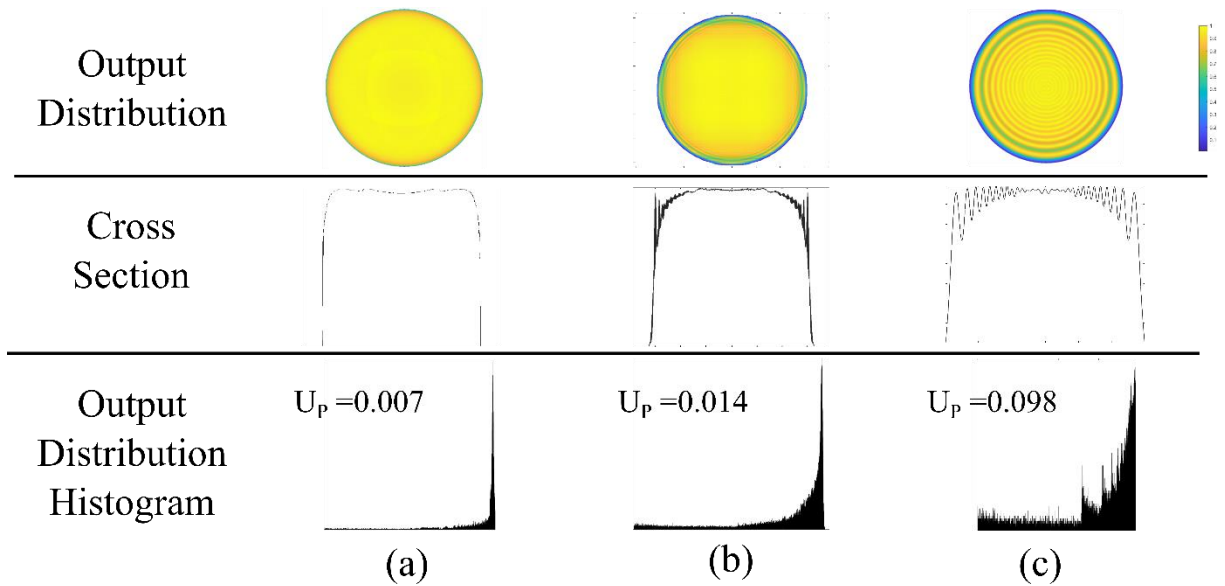
Fig. 4.5: Example distributions and UP terms

Simulations of all systems were performed in VirtualLab Fusion™ with the raw data of the outputs exported to MATLAB for analysis. In all systems the input distribution is a Gaussian beam with a 3 mm $1/e^2$ waist diameter. VirtualLab Fusion™ uses an automatic physical propagation method ("Field Tracing") which is a combination of Fourier Transform methods used for fast physical

propagation of light through the system. All afocal systems were simulated with the detector at 10 mm away from the last surface of the beam shaper.

4.4 Results

4.4.1 Achromatic Beam Shapers for Mid-wave Infrared Lasers (MWIR)

As our first system we explore a unique situation due to material properties. Silicon has a nearly constant index of refraction for 3 to 5 µm, avoiding the need for achromatic correction. We used a target output distribution of uniform irradiance of a square with a side length of 4 mm. The focal freeform system was designed for a focal length of 20 mm and the afocal system with a separation of 20 mm. Surface coefficients, radius of curvature R, element diameter D, surface separation d, and element material are listed in Tables 4.1 and 4.2. Surface coefficients for first and, if applicable, second freeform surfaces follow the convention of Equation 4.18 where k is equal to integers 1 through 7.

$$z(x, y) = \sum a_{2k}(x^{2k} + y^{2k})$$
$$Z(X,Y) = \sum A_{2k}(X^{2k} + Y^{2k})$$

(4.18)

Fig. 4.6: MWIR Freeform Focal Beam Shaper

Table 4.1: Surface Data (Figure 4.6)

Surface #	R (mm)	D (mm)	d (mm)	Material	Surface Coefficients: a_{2k} (mm^{1-2k})
1	Infinity	3	1.0	Silicon	
2	Infinity	3	20		a_2= 4.43E-02; a_4= -7.84E-03; a_6= 1.16E-03; a_8= -1.66E-04; a_{10}= 2.27E-05; a_{12}= -2.50E-06; a_{14}= 1.49E-07;

Fig. 4.7: MWIR Freeform Afocal Beam Shaper

Table 4.2: Surface Data (Figure 4.7)

Surface #	R (mm)	D (mm)	d (mm)	Material	Surface Coefficients: a_{2k} and A_{2k} (mm^{1-2k})
1	Infinity	3	1.0	Silicon	
2	Infinity	3	20		a_2= -7.83E-02; a_4= -6.52E-05; a_6= 1.82E-05; a_8= -8.55E-07; a_{10}= 3.15E-08; a_{12}= -9.30E-10; a_{14}= 1.64E-11;
3	Infinity	8	1.0	Silicon	A_2= -7.83E-02; A_4= -6.52E-05; A_6= 1.82E-05; A_8= -8.55E-07; A_{10}= 3.15E-08; A_{12}= -9.30E-10; A_{14}= 1.64E-11;
4	Infinity	8	10		

For the two systems in Tables 4.1 and 4.2 we have a standard deviation of output dimension

across source wavelengths of 0.02 mm which indicates achromatic performance with less than 1%

variation of the output dimension with respect to wavelength. However, there is a notable difference in the plateau uniformity, as illustrated in Figure 4.8.
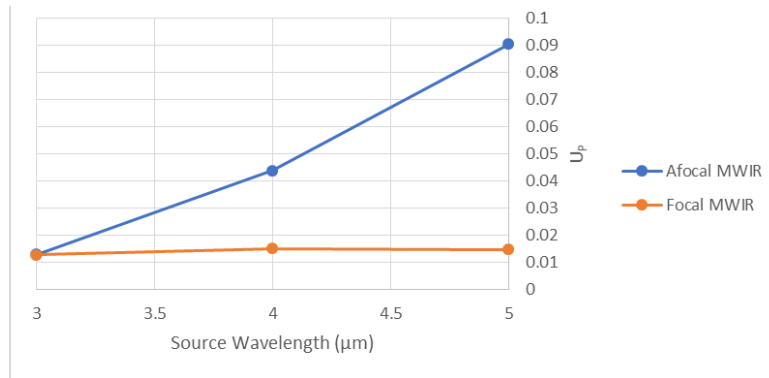
Fig. 4.8: UP vs λ (µm) for Focal and Afocal MWIR Freeform Systems

The addition of a second element for the afocal configuration appears to have increased the variation in uniformity, likely due to dispersion effects at longer source wavelengths and visibly evidenced by the ringing effect at the edge of the output distributions.

4.4.2 Supercontinuum Source Band – Beam Expansion

We next consider a broader source bandwidth corresponding to supercontinuum laser sources [118, 121]. Using a source wavelength set of 0.4 to 2.4 µm with a design wavelength of 1.55 µm we designed several freeform beam shapers [118, 120, 121]. We chose Schott N-FK51A (n_1) and KzFSN4 (n_2) materials for good secondary spectrum performance (in these cases 9.51 µm). We used a target output distribution of uniform irradiance of a square with a side length of 4 mm. The focal freeform systems were designed for a focal length of 20 mm and the afocal systems with a separation of 20 mm. System parameters are reported in Tables 4.3 through 4.8.

Gaussian Input
ω_o = 1.5 mm

Uniform Square Output
Side Length = 4 mm

Detector

δ = 0.04 mm

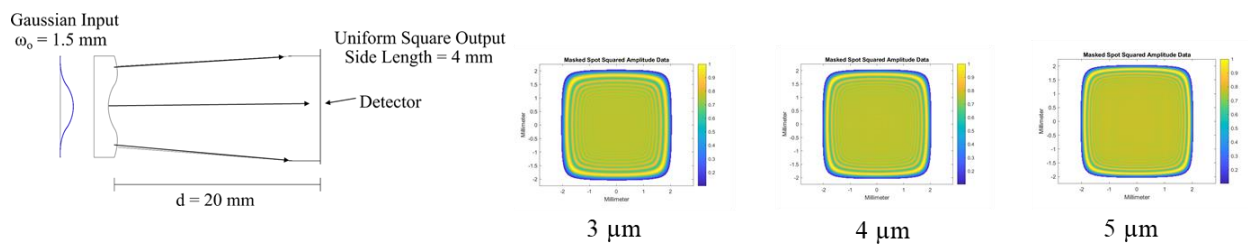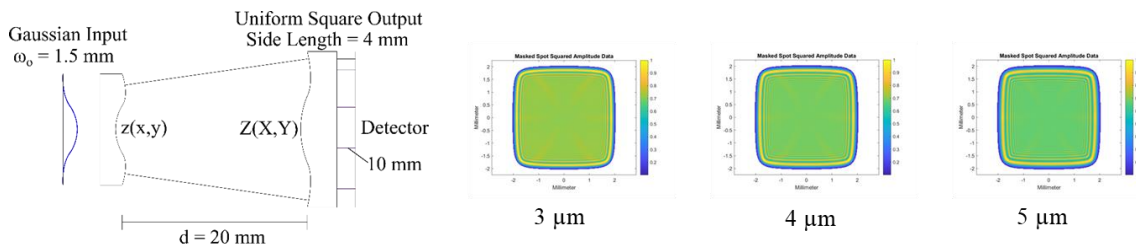Avg. U_P = 0.04

d = 20 mm

Fig. 4.9: Supercontinuum Freeform Focal Beam Shaper

Table 4.3: Surface Data (Figure 4.9)

Surface #	R (mm)	D (mm)	d (mm)	Material	Surface Coefficients: a_{2k} (mm^{1-2k})
1	Infinity	3	1.0	N-FK51A	
2	Infinity	3	20		a_2= 6.43E-02; a_4= -1.72E-02; a_6= 3.01E-03; a_8= -4.67E-04; a_{10}= 6.01E-05; a_{12}= - -5.79E-06; a_{14}= 3.04E-07;

Gaussian Input
ω_o = 1.5 mm

Radially symmetric
chromatic corrector

Uniform Square Output
Side Length = 4 mm

Detector

n1   n2

δ = 0.06 mm

Avg. U_P = 0.03

d = 20 mm

Fig. 4.10: Supercontinuum Achromatic Freeform Focal Beam Shaper – Radially Symmetric Chromatic Corrector

Table 4.4: Surface Data (Figure 4.10)

Surface #	R (mm)	D (mm)	d (mm)	Material	Surface Coefficients: a_{2k} (mm^{1-2k})
1	Infinity	3	1.0	N-FK51A	
2	Infinity	3	0.1		$a_2 = 7.98E\text{-}03$; $a_4 = -1.74E\text{-}02$; $a_6 = 3.08E\text{-}03$; $a_8 = -4.74E\text{-}04$; $a_{10} = 6.17E\text{-}05$; $a_{12} = -6.32E\text{-}06$; $a_{14} = 3.76E\text{-}07$;
3	-10.93	4.5	1.0	KzFSN4	
4	Infinity	4.5	20		

Fig. 4.11: Supercontinuum Achromatic Freeform Focal Beam Shaper – Freeform Chromatic Corrector

Table 4.5: Surface Data (Figure 4.11)

Surface #	R (mm)	D (mm)	d (mm)	Material	Surface Coefficients: a_{2k} and A_{2k} (mm^{1-2k})
1	Infinity	3	1.0	KzFSN4	
2	Infinity	3	0.1		a_2= 4.87E-02; a_4= -1.39E-02; a_6= 2.45E-03; a_8= -3.80E-04; a_{10}= 4.94E-05; a_{12}= -4.87E-06; a_{14}= 2.66E-07;
3	-10.93	4.5	1.0	N-FK51A	A_2= 2.25E-03; A_4= -9.40E-04; A_6= 1.67E-04; A_8= -2.63E-05; A_{10}= 3.46E-06; A_{12}= -3.43E-07; A_{14}= 1.86E-08;
4	Infinity	4.5	20		

For the focal systems above, the progression shows improvement as we go from only a focal beam shaping element which is already reasonably close to achromatic but demonstrates diffraction effects at the edges of the output as seen in Figure 4.9. The achromatic pairs building off of the achromatic doublet constraints results first, in Figure 4.10, in a slight improvement in uniformity with noticeable improvement in diffraction effects. Finally, applying the achromatic-doublet constraints to a second beam shaping surface we arrive at a system with no change in output dimension with respect to wavelength and good uniformity. The following two systems are afocal designs. The separation of the chromatic correction lens in Figure 4.13 was varied to determine the best output plane location considering both uniformity of output dimension and plateau irradiance.
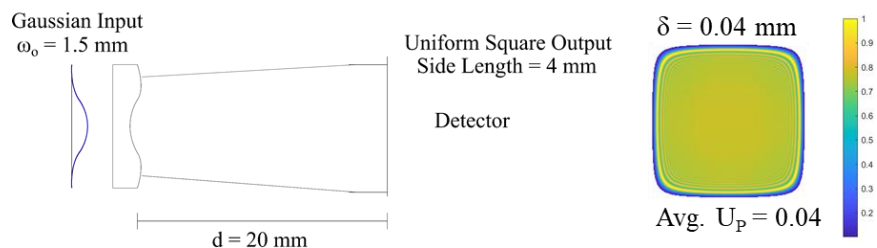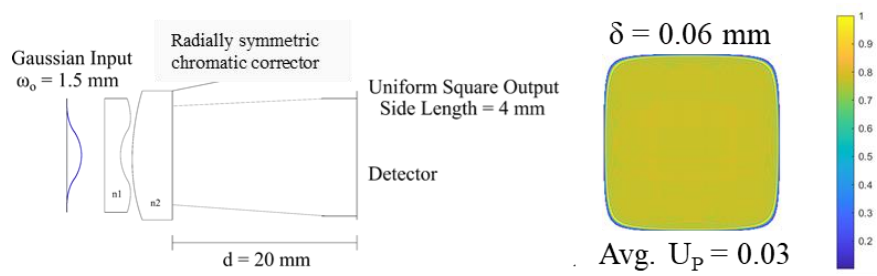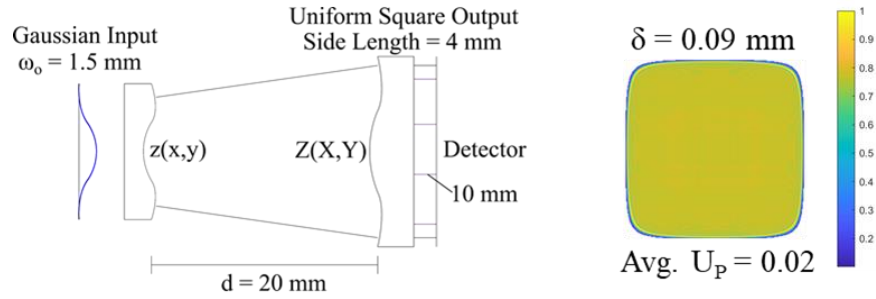
Fig. 4.12: Supercontinuum Freeform Afocal Beam Shaper

Table 4.6: Surface Data (Figure 4.12)

Surface #	R (mm)	D (mm)	d (mm)	Material	Surface Coefficients: a_{2k} and A_{2k} (mm^{1-2k})
1	Infinity	3	1.0	N-FK51A	
2	Infinity	3	20.0		a_2= 6.43E-02; a_4= -1.72E-02; a_6= 3.01E-03; a_8= -4.67E-04; a_{10}= 6.01E-05; a_{12}= -5.79E-06; a_{14}= 3.04E-07;
3	Infinity	4.5	1.0	N-FK51A	A_2= 2.88E-02; A_4= -5.02E-04; A_6= -4.09E-04; A_8= 3.17E-04; A_{10}= -1.53E-04; A_{12}= - 3.48E-05; A_{14}= -3.19E-06;
4	Infinity	4.5	10		

Here we illustrate the broadband functionality by variation of the separation of the afocal system in Figure 4.12. The system is not perfectly achromatic but, by changing the separation between the beam shaping elements we can demonstrate broadband functionality at specific configurations of the system as seen in Figure 4.13.
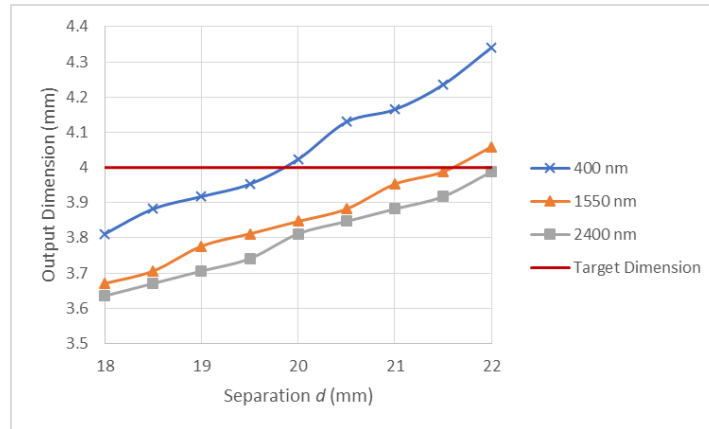
Fig. 4.13: Output Square Side Length versus Separation d (System of Figure 12)
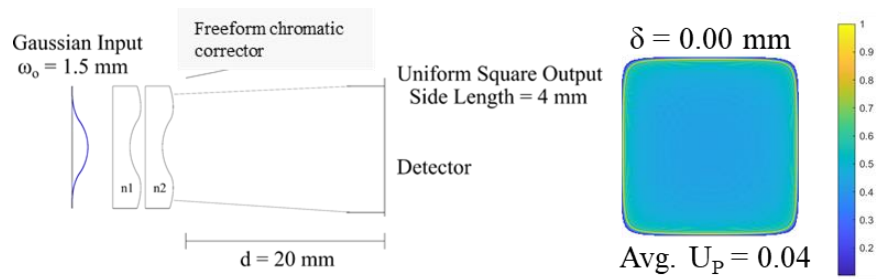

Fig. 4.14: Supercontinuum Achromatic Freeform Afocal Beam Shaper – Radially Symmetric Chromatic Corrector

Table 4.7: Surface Data (Figure 4.14)

Surface #	R (mm)	D (mm)	d (mm)	Material	Surface Coefficients: a_{2k} and A_{2k} (mm^{1-2k})
1	Infinity	3	1.0	N-FK51A	
2	Infinity	3	18.0		$a_2= 6.43E-02$; $a_4= -1.72E-02$; $a_6= 3.01E-03$; $a_8= -4.67E-04$; $a_{10}= 6.01E-05$; $a_{12}= -5.79E-06$; $a_{14}= 3.04E-07$;
3	20.92	4	1.0	KzFSN4	
4	23.93	4	1.0		
5	Infinity	4	1.0	N-FK51A	$A_2= 2.88E-02$; $A_4= -5.02E-04$; $A_6= -4.09E-04$; $A_8= 3.17E-04$; $A_{10}= -1.53E-04$; $A_{12}= - 3.48E-05$; $A_{14}= -3.19E-06$;
6	Infinity	4	10		

The achromatic afocal design results in Figure 4.14 are a slight improvement over the performance of the non-achromatic afocal system. Modifying the internal optical element to have at least one freeform surface may improve performance further but will require numerical design methods.

4.4.3 Supercontinuum Source Band – Beam Compression

The systems of Section 4.4.2 were all designed for beam expansion, or in other words a larger output dimension than input dimension. We now change our target output distribution of uniform irradiance to a square with a side length of 2 mm. The system shown in Figure 4.18 is a conventional radially symmetric output system described in the literature with known high quality

performance out to 1.064 µm. We added a square mask to mimic methods for generating square outputs using additional elements in order to compare our freeform systems to a conventional approach. Such a mask blocks at least 36% of the energy at the output. Our results shown in Figures 4.15 through 4.17 demonstrate comparable achromatic performance in output dimension. Figures 4.16 and 4.17 are in the range of uniformity performance for a masked system. Therefore we have three systems, two being compact in comparison to the afocal systems, capable of generating an achromatic compressed square beam without any loss of energy aside from material absorption.
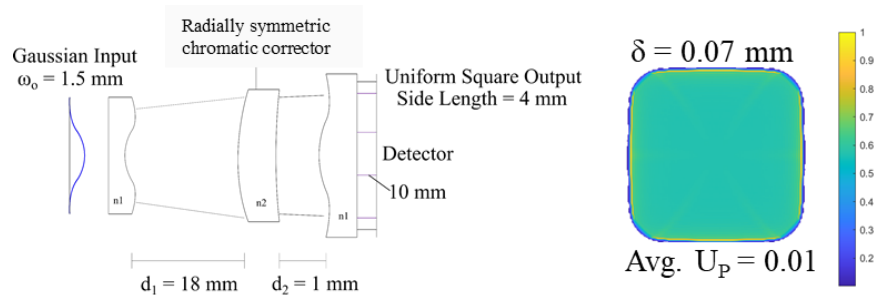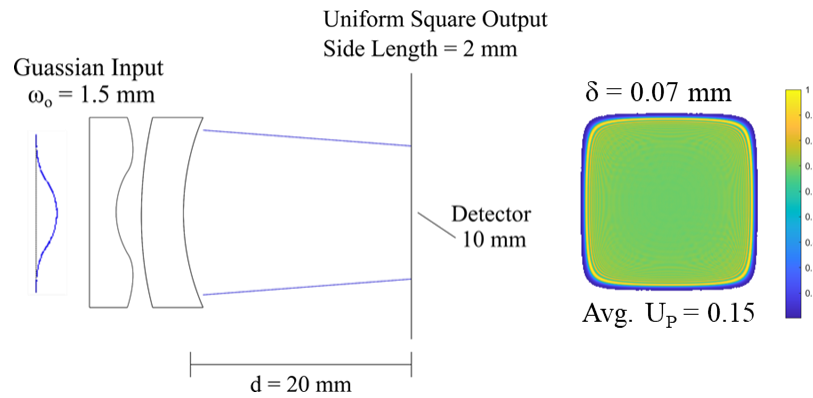

Fig. 4.15: Supercontinuum Achromatic Freeform Focal Beam Shaper – Radially Symmetric Chromatic Corrector

Table 4.8: Surface Data (Figure 4.15)

Surface #	R (mm)	D (mm)	d (mm)	Material	Surface Coefficients: a_{2k} (mm^{1-2k})
1	Infinity	3	1.0	N-FK51A	
2	Infinity	3	0.1		a_2= -5.14E-02; a_4= -8.67E-03; a_6= 1.61E-03; a_8= -2.51E-04; a_{10}= 3.25E-05; a_{12}= -3.13E-06; a_{14}= 1.64E-07;
3	-10.93	3	1.0	KzFSN4	
4	Infinity	3	20		
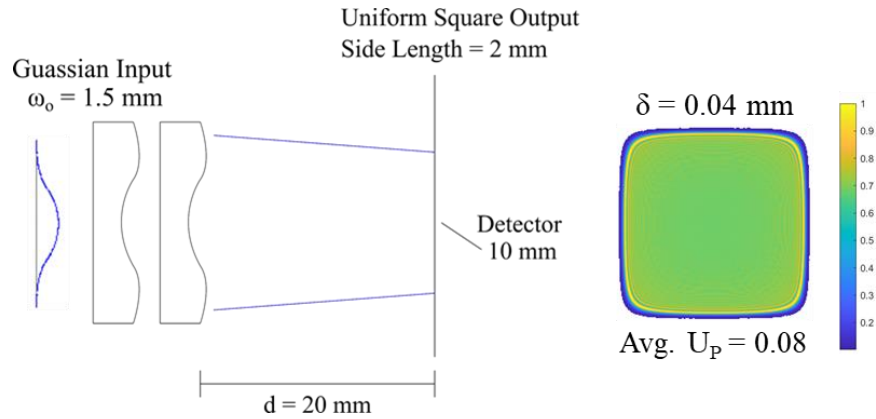
Fig. 4.16: Supercontinuum Achromatic Freeform Focal Beam Shaper – Freeform Chromatic Corrector

Table 4.9: Surface Data (Figure 4.16)

Surface #	R (mm)	D (mm)	d (mm)	Material	Surface Coefficients: a_{2k} and A_{2k} (mm^{1-2k})
1	Infinity	3	1.0	KzFSN4	
2	Infinity	3	0.1		$a_2 = 1.56E\text{-}03$; $a_4 = -7.02E\text{-}03$; $a_6 = 1.25E\text{-}03$; $a_8 = -1.95E\text{-}04$; $a_{10} = 2.55E\text{-}05$; $a_{12} = -2.50E\text{-}06$; $a_{14} = 1.35E\text{-}07$;
3	Infinity	3	1.0	N-FK51A	$A_2 = 4.94E\text{-}03$; $A_4 = -1.34E\text{-}03$; $A_6 = 2.38E\text{-}04$; $A_8 = -3.74E\text{-}05$; $A_{10} = 4.93E\text{-}06$; $A_{12} = -4.88E\text{-}07$; $A_{14} = 2.65E\text{-}08$;
4	Infinity	3	20		

Fig. 4.17: Supercontinuum Achromatic Freeform Focal Beam Shaper – Freeform Chromatic Corrector

Table 4.10: Surface Data (Figure 4.17)

Surface #	R (mm)	D (mm)	d (mm)	Material	Surface Coefficients: a_{2k} and A_{2k} (mm^{1-2k})
1	Infinity	3	1.0	N-FK51A	
2	Infinity	3	18.0		a_2= 6.43E-02; a_4= -1.72E-02; a_6= 3.01E-03; a_8= -4.67E-04; a_{10}= 6.01E-05; a_{12}= -5.79E-06; a_{14}= 3.04E-07;
3	9.12	3	1.0	KzFSN4	
4	11.97	3	1.0		
5	Infinity	2.5	1.0	N-FK51A	A_2= 2.88E-02; A_4= -5.02E-04; A_6= -4.09E-04; A_8= 3.17E-04; A_{10}= -1.53E-04; A_{12}= - 3.48E-05; A_{14}= -3.19E-06;
6	Infinity	2.5	10		
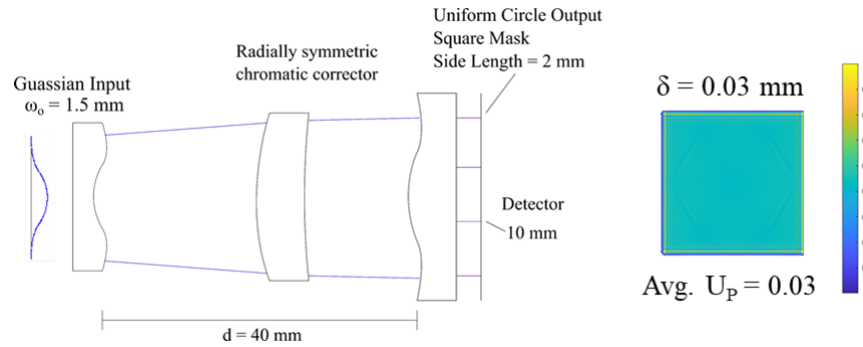
Fig. 4.18: Laskin Afocal Achromatic Beam Shaper with Square Mask [29]

Figure 4.19 summarizes the performance of the above systems, demonstrating that the achromatic freeform beam shapers meet or exceed the uniformity of a masked conventional beam shaper, indicating that the above systems are useful replacements for conventional square beam shapers.
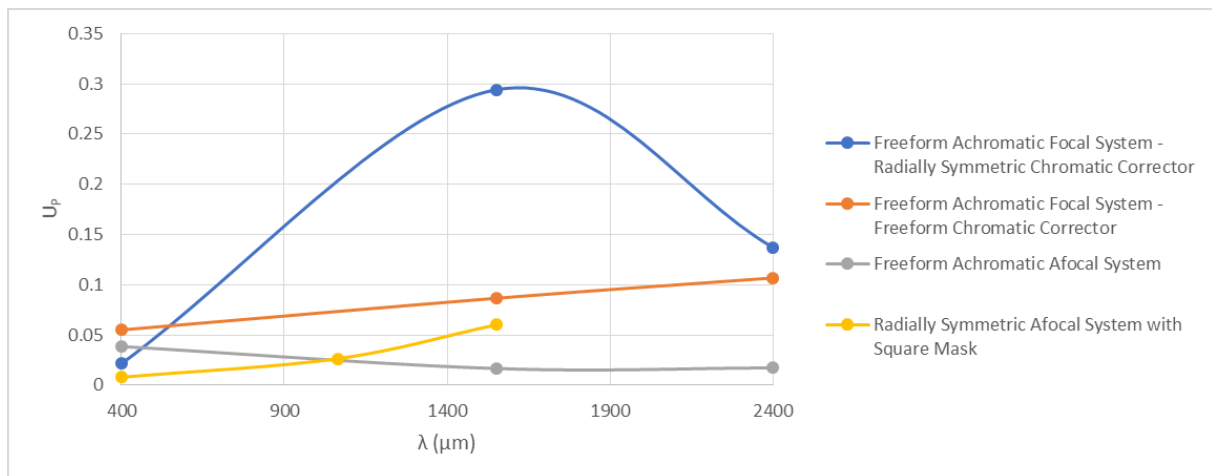
Fig. 4.19: U_P versus Source Wavelength

4.5 Conclusion

We have presented several designs of achromatic and broadband capable freeform beam shaping systems with a goal of achieving non-radial output distributions without requiring additional optical elements or significant loss of energy. We have also presented simulated results for several different configurations spanning bandwidths from the visible to the mid-wave infrared.

By using a focal system we can reduce the number of components needed, compared to afocal and conventional beam shapers and reduce the overall system scale providing a more compact option albeit with a limited range of functionality compared to the afocal versions. Future work to improve the design methodology of achromatic focal beam shapers will include considering truly cemented systems of matching freeform surfaces. This may aid in further improving the performance of the focal systems. Further, numerical methods to include freeform surfaces in the chromatic correction of afocal systems should be investigated. Other non-radial output distributions than squares would also be beneficial for consideration to demonstrate broader freeform capabilities.

REFERENCE LIST

1.   Geary, Joseph M. *Introduction to Lens Design: With Practical Zemax Examples.* Willmann-Bell Richmond, VA, USA:, 2002.

9.   Flores, Angel et al. "Achromatic Hybrid Refractive-Diffractive Lens with Extended Depth of Focus." *Applied optics*, vol. 43, no. 30, 2004, pp. 5618-30.

15. Schulz, Gunter. "Achromatic and Sharp Focussing of Laser Beams by Aspherics." *Symposium Optika'84*, vol. 473, 1985, pp. 238-41.

20. Valley, Pouria et al. "Adjustable Hybrid Diffractive/Refractive Achromatic Lens." *Optics express*, vol. 19, no. 8, 2011, pp. 7468-79.

28. Jefferson, C Michael and John A Hoffnagle. "An Achromatic Refractive Laser Beam Reshaper." *Proc. SPIE*, *Laser Beam Shaping IV*, vol. 5175, 2003, pp. 1-11.

29. Laskin, Alexander. "Achromatic Refractive Beam Shaping Optics for Broad Spectrum Laser Applications." *Proc. SPIE, Laser Beam Shaping X*, vol. 7430, 2009, p. 743003.

30. Laskin, Alexander and David Shealy. "Building Achromatic Refractive Beam Shapers." *Proc. SPIE, Laser Beam Shaping XV*, vol. 9194, 2014, p. 91940R.

33. Möhl, A et al. "Gauss to Top-Hat Beam Shaping with Aspheres." *Proc. SPIE, High-Power Laser Materials Processing: Lasers, Beam Delivery, Diagnostics, and Applications V*, vol. 9741, 2016, p. 974102.

43. Rosete-Aguilar, M., J. Garduño-Mejía, and N. C. Bruce. "Focusing ultrashort laser pulses with achromatic doublets." SPIE Newsroom (2015): 1-3.

44. Hoffnagle, John A and C Michael Jefferson. "Design and Performance of a Refractive Optical System That Converts a Gaussian to a Flattop Beam." *Applied optics*, vol. 39, no. 30, 2000, pp. 5488-99.

58. Smilie, Paul J et al. "Design and Characterization of an Infrared Alvarez Lens." *Optical Engineering*, vol. 51, no. 1, 2012, p. 013006.

59. Wu, Rengmao et al. "The Monge-Ampère Equation Design Method and Its Application to Beam Shaping." *Imaging and Applied Optics 2015*, Optica Publishing Group, 2015/06/07 2015, p. FTh3B.1. *OSA Technical Digest (online)*, doi:10.1364/FREEFORM.2015.FTh3B.1.

60. Shultz, Jason A et al. "Experimental Characterization of Variable Output Refractive Beamshapers Using Freeform Elements." *Proc. SPIE, Laser Beam Shaping XV*, vol. 9194, 2014, p. 91940M.

61.   Suleski, Thomas J et al. "Dynamic Beam Shaping with Freeform Optics." *Proc. SPIE, Laser Beam Shaping XV*, vol. 9194, 2014, p. 91940K.

62.   Zhang, Yaqin et al. "Double Freeform Surfaces Design for Laser Beam Shaping with Monge–Ampère Equation Method." *Optics Communications*, vol. 331, 2014, pp. 297-305.

69.   Malyak, Phillip H. "Two-Mirror Unobscured Optical System for Reshaping the Irradiance Distribution of a Laser Beam." *Applied optics*, vol. 31, no. 22, 1992, pp. 4377-83.

78.   Dickey, Fred M and Scott C Holswade. *Laser Beam Shaping.* Marcel Dekker New York, 2000.

79.   Rhodes, Patrick W. and David L. Shealy. "Refractive Optical Systems for Irradiance Redistribution of Collimated Radiation: Their Design and Analysis." *Applied optics*, vol. 19, no. 20, 1980, pp. 3545-53, doi:10.1364/AO.19.003545.

80.   Dickey, Fred M. "Laser Beam Shaping." *Optics and Photonics News*, vol. 14, no. 4, 2003, pp. 30-35.

81.   Dickey, Fred M et al. "Laser Beam Shaping Techniques." *Proc. SPIE, High-Power Laser Ablation III*, vol. 4065, 2000, pp. 338-48.

82.   Ding, Li et al. "Broadband Beam Shaping Using Two Cascaded Diffractive Optical Elements with Different Sizes of Effective Phase Region." *Proc. SPIE, AOPC 2017: Optoelectronics and Micro/Nano-Optics*, vol. 10460, 2017, p. 1046004.

84.   Veldkamp, Wilfrid B. "Technique for Generating Focal-Plane Flattop Laser-Beam Profiles." *Review of Scientific Instruments*, vol. 53, no. 3, 1982, pp. 294-97.

86.   Oliker, Vladimir. "On Design of Free-Form Refractive Beam Shapers, Sensitivity to Figure Error, and Convexity of Lenses." *JOSA A*, vol. 25, no. 12, 2008, pp. 3067-76.

87.   Laskin, Alexander and Vadim Laskin. "Beam Shaping to Generate Uniform Laser Light Sheet and Linear Laser Spots." *Proc. SPIE, Laser Beam Shaping XIV*, vol. 8843, 2013, p. 88430C.

88.   Laskin, Alexander et al. "Square Shaped Flat-Top Beam in Refractive Beam Shapers." *Proc. SPIE, Laser Beam Shaping XVI*, vol. 9581, 2015, p. 95810K.

89.   Laskin, Alexander. "Solutions for Beam Shaping: Control of Laser Intensity Profile and Spot Shape with Refractive Beam Shaping." *Laser Technik Journal*, vol. 10, no. 1, 2013, pp. 37-40.

90.   Laskin, Alexander and Vadim Laskin. "Variable Beam Shaping with Using the Same Field Mapping Refractive Beam Shaper." *Proc. SPIE, Laser Resonators, Microresonators, and Beam Control XIV*, vol. 8236, 2012, p. 82360D.

92.   Möhl, A et al. "Modular Optical Design for Flexible Beam Shaping of a Top-Hat Profile." *Proc. SPIE, Optical Systems Design 2015: Optical Design and Engineering VI*, vol. 9626, 2015, p. 96261W.

96.   Kukhtarev, Nickolai V et al. "Laser Beam Shaping by Holographic Optical Elements." *Proc. SPIE, Ninth International Conference on Nonlinear Optics of Liquid and Photorefractive Crystals*, vol. 5257, 2003, pp. 152-62.

97.   Račiukaitis, Gediminas et al. "Laser Processing by Using Diffractive Optical Laser Beam Shaping Technique." *Journal of laser micro/nanoengineering*, vol. 6, no. 1, 2011.

100.   Shultz, Jason Allen. "Design, Tolerancing, and Experimental Characterization of Dynamic Freeform Optical Systems." PhD Dissertation, The University of North Carolina at Charlotte, 2017.

118.   Alfano, Robert R. "The Supercontinuum Laser Source." *The Supercontinuum Laser Source: The Ultimate White Light, ISBN 978-1-4939-3324-2. Springer Science+ Business Media New York*, 2016.

120.   Granzow, Nicolai. "Supercontinuum White Light Lasers: A Review on Technology and Applications." *Proc. SPIE, Joint TC1 - TC2 International Symposium on Photonics and Education in Measurement Science 2019*, vol. 11144, SPIE, 2019. https://doi.org/10.1117/12.2533094.

121.   Singh, Manisha et al. "Beam Shaping of Supercontinuum Pulses." *Proc. SPIE, Optical Systems Design 2015: Optical Design and Engineering VI*, vol. 9626, 2015, p. 962633.

135.   Romero, Louis and Fred M Dickey. "What Makes a Beam Shaping Problem Difficult." Sandia National Labs., 2000.

136.   Duerr, Fabian and Hugo Thienpont. "Direct Design of Laser-Beam Shapers, Zoom-Beam Expanders, and Combinations Thereof." *Proc. SPIE, Optical Design and Testing VII*, vol. 10021, 2016, p. 100210K.

137.   Hoffnagle, John A and C Michael Jefferson. "Beam Shaping with a Plano-Aspheric Lens Pair." *Optical Engineering*, vol. 42, no. 11, 2003, pp. 3090-99.

138.   Laskin, Alexander and Vadim Laskin. "Refractive Field Mapping Beam Shaping Optics: Important Features for a Right Choice." *International Congress on Applications of Lasers & Electro-Optics*, vol. 2010, Laser Institute of America, 2010, pp. 1181-89.

139. Laskin, Alexander and David Shealy. "Designing Refractive Beam Shapers Via Aberration Theory." *Proc. SPIE, Laser Beam Shaping XV*, vol. 9194, 2014, p. 91940T.

140. Laskin, Alexander et al. "Applying Refractive Beam Shapers in Creating Spots of Uniform Intensity and Various Shapes." *Proc. SPIE, Laser Resonators and Beam Control XII*, vol. 7579, 2010, p. 75790N.

141. Shealy, David L and Shao-Hua Chao. "Geometric Optics-Based Design of Laser Beam Shapers." *Optical Engineering*, vol. 42, no. 11, 2003, pp. 3123-38.

142. Shealy, David L and John A Hoffnagle. "Design and Analysis of Plano-Aspheric Laser Beam Shapers." *Proc. SPIE, Laser Beam Shaping XIII*, vol. 8490, 2012, p. 849003.

143. Shealy, David L and John A Hoffnagle. "Laser Beam Shaping Profiles and Propagation." *Applied optics*, vol. 45, no. 21, 2006, pp. 5118-31.

144. Hoffnagle, John A and David L Shealy. "Optical and Mechanical Tolerances for Two-Lens Plano-Aspheric Laser Beam Shapers." *Proc. SPIE, Laser Beam Shaping XIII*, vol. 8490, 2012, p. 849004.

145. ten Thije Boonkkamp, J. H. M. et al. "The Monge-Ampère Equation for Freeform Optics." *Imaging and Applied Optics 2015*, Optica Publishing Group, 2015/06/07 2015, p. FTh3B.4. *OSA Technical Digest (online)*, doi:10.1364/FREEFORM.2015.FTh3B.4.

146. Jiang, Wu et al. "Design and Testing of a Refractive Reshaping System." *Proc. SPIE, 1993 International Symposium on Optics, Imaging, and Instrumentation*, vol. 2000, 1993, OP. https://doi.org/10.1117/12.163670.

147. Zhang, S. et al. "Single-Element Laser Beam Shaper for Uniform Flat-Top Profiles." *Optics express*, vol. 11, no. 16, 2003, pp. 1942-48, doi:10.1364/OE.11.001942.

148. Smilie, Paul Joseph. "Dynamic Optical Systems through Laterally Translated Refractive Freeform Elements." University of North Carolina at Charlotte, 2011.

149. Mann, Klaus R et al. "Characterization of Excimer Laser Beam Parameters." *Proc. SPIE, Third International Workshop on Laser Beam and Optics Characterization*, vol. 2870, 1996, pp. 367-77.

150. ISO. "Optics and Photonics - Lasers and Laser-Related Equipment - Test Methods for Laser Beam Power (Energy) Density Distribution." vol. 13694, 2018.

CHAPTER 5: CONCLUSION

5.1 Summary and Comparisons

Two sets of freeform optical systems for broadband functionality have been presented in this dissertation. Initial designs of BVTS systems in Chapters 2 and 3 and achromatic beam shapers for non-radially symmetric outputs in Chapter 4 were presented and their functions simulated. In both cases, results were compared across source wavelengths for characterizing the broadband optical performance of the freeform-enabled systems. The primary advantage of each system presented is the enabling of broadband functionality for applications which otherwise are otherwise not available.

The BVTS systems as presented function within our targets for the longer source wavelengths. This indicates that the BVTS system should be able to retrieve surface information from curved surfaces being measured with Fizeau interferometry. Further, the BVTS systems for the longer source wavelengths function for a broad range of f-numbers, enabling the potential replacement of 10's of conventional transmission spheres with one BVTS. Further, due to nearly continuous functionality within the range of source wavelengths and f-numbers, the BVTS can be used for many other source wavelengths and f-numbers not explicitly considered in this work.

The work reported in Chapter 4 combines freeform beam shaping principles with achromatic and broadband beam shaping concepts to achieve broadband functionality for simple non-radially symmetric output distributions. Systems are reported for both focal and afocal methods across a broad spectral range. It should be noted that the beam shaping problem is harder for longer source wavelengths due to diffractive effects on beam propagation, resulting in a 'ringing' effect. The freeform achromatic beam shaping problem is more straightforward in the MWIR spectrum due to the nearly constant index of refraction of silicon in the chosen wavelength band; the higher

performance quality for the MWIR case compared to other source wavelength ranges is due in part to the lack of need of a chromatic aberration correcting element. This indicates that if optical designers can find (or, using metamaterial concepts, design) materials with minimal dispersion across the range of source wavelengths, it should be possible to achieve high quality achromatic beam shaping with simplified constraints.

In the case of the BVTS systems as discussed in Chapters 2 and 3, the systems can function for any source wavelength for which the optical material is transmissive by utilizing discrete lateral relative shifts of the freeform elements. Chapter 4 leverages a similar concept through longitudinal relative shifts of the elements along the optical axis to achieve broadband beam shaping of square outputs in afocal systems. In both cases, the change in position of the optical elements can be related by Equation 5.1 where d_i is either the lateral translation of the BVTS elements or the axial separation of the afocal beam shaping elements.

$$d_2 = d_1 \frac{n(\lambda_1) - 1}{n(\lambda_2) - 1} \tag{5.1}$$

The use of this same equation for two types of broadband functionality with freeform surfaces may be useful for future consideration of other application spaces.

5.2 Future Work

5.2.1 Optical Designs and Simulation

1. One primary conclusion from the systems in this dissertation is the imperfections and challenges produced by freeform surfaces. In the case of the BVTS systems, further work is needed on optimization metrics and methods that directly relate the design and optimization of surface parameters to retrace error performance. In particular, as noted in Chapter 3,

developing an optimization method wherein a BVTS is optimized as part of a simulated Fizeau interferometer for ideal surfaces may improve system performance.

2. The BVTS systems explored were for very broad ranges of source wavelengths to study general principles of the systems. Future research into alternative materials and source wavelength ranges could further improve measurement capabilities of BVTS systems.

3. The BVTS has potential to be used for the measurement of surfaces with significant spatial variation in surface curvature with the part aperture (such as freeforms or examples like gull-wing aspheres). These applications should be taken into consideration when designing, optimizing, and simulating future BVTS systems.

4. Freeform achromatic transmissive beam shapers as discussed in Chapter 4 may also benefit from improved optimization methods and alternative system parameters.

5. For the achromatic focal beam shaping systems identifying a method by which two planar-freeform elements of different materials but the same freeform surface cemented together could result in better achromatic beam shaping in a focal plane for a compact system.

6. The square output distributions demonstrated are relatively simple; future designs could include investigating achromatic performance for more complex output distributions such as logos, letters, or non-uniform distributions.

5.2.2 Fabrication and Testing

1. The BVTS and beam shaping systems discussed in were simulated while fabrication and experimental tests have yet to be performed. It will be important to identify necessary surface finishes and tolerances before fabrication, as well as system parameters appropriate to available lab equipment.

2. Special attention will need to be paid to experimental implementation of the BVTS surfaces, alignment, and lateral translation systems as deviations will result in greater retrace error.

3. The beam shaping surfaces require less consideration but will still require appropriate surface finishes to avoid diffraction effects as well as appropriate mounting and alignment. Since the surfaces of the afocal freeform beam shapers are not radially symmetric it will be important to ensure proper rotational alignment of the surfaces with respect to each other.

REFERENCES

1. Geary, Joseph M. *Introduction to Lens Design: With Practical Zemax Examples.* Willmann-Bell Richmond, VA, USA:, 2002.

2. Dittman, Michael G et al. "Limb Broadband Imaging Spectrometer for the Npoess Ozone Mapping and Profiler Suite (Omps)." *Proc. SPIE, Earth Observing Systems VII*, vol. 4814, 2002, pp. 120-30.

3. Holfort, Iben Kraglund et al. "Broadband Minimum Variance Beamforming for Ultrasound Imaging." *Proceedings of the IEEE*, vol. 56, no. 2, 2009, pp. 314-25.

4. Spector, SJ et al. "Broadband Imaging and Wireless Communication with an Optical Phased Array." *CLEO: Science and Innovations*, Optical Society of America, 2018, p. SM3I. 7.

5. Bagwell, Joel et al. "An Achromat Singlet." *Proc. SPIE, Components and Packaging for Laser Systems VI,* vol. 11261, 2020, p.1126110.

6. Biraud, F and G Daigne. "Achromatic Doublets for Gaussian Beams." *Proceedings of the IEEE, transactions on antennas and propagation*, vol. 39, no. 4, 1991, pp. 559-62.

7. Deng, Lijin et al. "True-Color Restoration of Reconstructed Image in Naked-Eye 3d Led Display Based on Eliminating Optical Dispersion." *Japanese Journal of Applied Physics*, vol. 59, no. 1, 2020, p. 017001.

8. Fernandez, Enrique J and Pablo Artal. "Achromatic Doublet Intraocular Lens for Full Aberration Correction." *Biomedical optics express*, vol. 8, no. 5, 2017, pp. 2396-404.

9. Flores, Angel et al. "Achromatic Hybrid Refractive-Diffractive Lens with Extended Depth of Focus." *Applied optics*, vol. 43, no. 30, 2004, pp. 5618-30.

10. Galan, M et al. "Design Method for Compact, Achromatic, High-Performance, Solid Catadioptric System (Socats), from Visible to Ir." *Optics express*, vol. 27, no. 1, 2019, pp. 142-49.

11. Jaecks, Duane H. "An Investigation of the Eighteenth-Century Achromatic Telescope." *Annals of science*, vol. 67, no. 2, 2010, pp. 149-86.

12. Levi, Leo. "A One-Glass Achromatic Doublet." *Optica Acta: International Journal of Optics*, vol. 27, no. 11, 1980, pp. 1491-97.

13. Oliva, E and S Gennari. "Achromatic Lens Systems for near Infrared Instruments." *Astronomy and Astrophysics Supplement Series*, vol. 114, 1995, p. 179.

14.   Reichelt, Stephan and Hans Zappe. "Design of Spherically Corrected, Achromatic Variable-Focus Liquid Lenses." *Optics express*, vol. 15, no. 21, 2007, pp. 14146-54.

15.   Schulz, Gunter. "Achromatic and Sharp Focussing of Laser Beams by Aspherics." *Symposium Optika'84*, vol. 473, 1985, pp. 238-41.

16.   Steel, WH. "On the Choice of Glasses for Cemented Achromatic Aplanatic Doublets." *Australian Journal of Physics*, vol. 7, no. 2, 1954, pp. 244-53.

17.   Strong, J. "Achromatic Doublet Lenses for Infrared Radiation." *Applied optics*, vol. 10, no. 6, 1971, pp. 1439-43.

18.   Treuting, RG. "An Achromatic Doublet of Silicon and Germanium." *JOSA*, vol. 41, no. 7, 1951, pp. 454-56.

19.   Vallerotto, Guido et al. "Experimental Characterization of Achromatic Doublet on Glass (Adg) Fresnel Lenses." *AIP Conference Proceedings*, vol. 1881, AIP Publishing LLC, 2017, p. 030010.

20.   Valley, Pouria et al. "Adjustable Hybrid Diffractive/Refractive Achromatic Lens." *Optics express*, vol. 19, no. 8, 2011, pp. 7468-79.

21.   Wang, Yan et al. "Design of Multi-Wavelength Achromatic Transmission Sphere Based on Zoom Principle." *Proc. SPIE*, *Optical Metrology and Inspection for Industrial Applications VII*, vol. 11552, 2020, p. 1155217.

22.   Cossel, Kevin C et al. "Gas-Phase Broadband Spectroscopy Using Active Sources: Progress, Status, and Applications." *JOSA B*, vol. 34, no. 1, 2017, pp. 104-29.

23.   Feike, Mea et al. "Broadband Multiple-Quantum Nmr Spectroscopy." *Journal of Magnetic Resonance, Series A*, vol. 122, no. 2, 1996, pp. 214-21.

24.   Fischer, Bernd M et al. "Chemical Recognition with Broadband Thz Spectroscopy." *Proceedings of the IEEE*, vol. 95, no. 8, 2007, pp. 1592-604.

25.   Thorpe, Michael J et al. "Broadband Cavity Ringdown Spectroscopy for Sensitive and Rapid Molecular Detection." *Science*, vol. 311, no. 5767, 2006, pp. 1595-99.

26.   Li, Can et al. "Optical System Design of Multispectral Achromatic Imaging Flow Cytometer." *Acta Optica Sinica*, vol. 36, no. 9, p. 0922002.

27.   Zhang, Wenqiang et al. "Light-Scattering Sizing of Single Submicron Particles by High-Sensitivity Flow Cytometry." *Analytical chemistry*, vol. 90, no. 21, 2018, pp. 12768-75.

28.   Jefferson, C Michael and John A Hoffnagle. "An Achromatic Refractive Laser Beam Reshaper." *Proc. SPIE*, *Laser Beam Shaping IV*, vol. 5175, 2003, pp. 1-11.

29. Laskin, Alexander. "Achromatic Refractive Beam Shaping Optics for Broad Spectrum Laser Applications." *Proc. SPIE, Laser Beam Shaping X*, vol. 7430, 2009, p. 743003.

30. Laskin, Alexander and David Shealy. "Building Achromatic Refractive Beam Shapers." *Proc. SPIE, Laser Beam Shaping XV*, vol. 9194, 2014, p. 91940R.

31. Bernges, Joerg et al. "Mask-Adapted Beam Shaping for Materials Processing with Excimer Laser Radiation." *Proc. SPIE, OPTIKA'98: 5th Congress on Modern Optics*, vol. 3573, 1998, pp. 108-11.

32. Flamm, Daniel et al. "Beam Shaping for Ultrafast Materials Processing." *Proc. SPIE, Laser Resonators, Microresonators, and Beam Control XXI*, vol. 10904, 2019, p. 109041G.

33. Möhl, A et al. "Gauss to Top-Hat Beam Shaping with Aspheres." *Proc. SPIE, High-Power Laser Materials Processing: Lasers, Beam Delivery, Diagnostics, and Applications V*, vol. 9741, 2016, p. 974102.

34. Bösel, Christoph and Herbert Gross. "Double Freeform Illumination Design for Prescribed Wavefronts and Irradiances." *JOSA A*, vol. 35, no. 2, 2018, pp. 236-43.

35. Feng, Zexin et al. "Freeform Illumination Optics Construction Following an Optimal Transport Map." *Applied optics*, vol. 55, no. 16, 2016, pp. 4301-06.

36. Ma, Donglin et al. "Freeform Illumination Lens Design Using Composite Ray Mapping." *Applied optics*, vol. 54, no. 3, 2015, pp. 498-503.

37. Shadalou, Shohreh and Thomas J Suleski. "Freeform Optics for Dynamic Illumination." *Proc. SPIE, Nonimaging Optics: Efficient Design for Illumination and Solar Concentration XVII*, vol. 11495, 2020, p. 114950B.

38. Wu, Rengmao et al. "Design of Freeform Illumination Optics." *Laser & Photonics Reviews*, vol. 12, no. 7, 2018, p. 1700310.

39. Effenberger, Frank J et al. "Advances in Broadband Passive Optical Networking Technologies." *Proceedings of the IEEE, Communications Magazine*, vol. 39, no. 12, 2001, pp. 118-24.

40. Xie, Zhenwei et al. "Ultra-Broadband on-Chip Twisted Light Emitter for Optical Communications." *Light: Science & Applications*, vol. 7, no. 4, 2018, pp. 18001-01.

41. Dokland, Terje. *Techniques in Microscopy for Biomedical Applications.* vol. 2, World Scientific, 2006.

42.   Beadie, Guy et al. "Materials Figure of Merit for Achromatic Gradient Index (Grin) Optics." *Proc. SPIE, Advanced Optics for Defense Applications: UV through LWIR*, vol. 9822, 2016, p. 98220Q.

43.   Rosete-Aguilar, M., J. Garduño-Mejía, and N. C. Bruce. "Focusing ultrashort laser pulses with achromatic doublets." SPIE Newsroom (2015): 1-3.

44.   Hoffnagle, John A and C Michael Jefferson. "Design and Performance of a Refractive Optical System That Converts a Gaussian to a Flattop Beam." *Applied optics*, vol. 39, no. 30, 2000, pp. 5488-99.

45.   Zhang, Xu et al. "Design and Analysis of Wide-Band Transmission Spheres for Multiwavelength Interferometers." *Optical Engineering*, vol. 60, no. 8, 2021, p. 085102, https://doi.org/10.1117/1.OE.60.8.085102.

46.   Lu, Qi et al. "A Simple High-Precision Wide-Spectrum Interferometric System." *Review of Scientific Instruments*, vol. 90, no. 7, 2019, p. 075109.

47.   Hayes, John. "Chromatic compensation in Fizeau interferometer." U.S. Patent No. 7,580,135. 25 Aug. 2009.

48.   Blalock, Todd et al. "Fabrication of Freeform Optics." *Proc. SPIE, Optical Engineering + Applications*, vol. 9575, 2015, https://doi.org/10.1117/12.2188523.

49.   Rolland, Jannick P et al. "Freeform Optics for Imaging." *Optica*, vol. 8, no. 2, 2021, pp. 161-76.

50.   Thompson, Kevin P and Jannick P Rolland. "Freeform Optical Surfaces: A Revolution in Imaging Optical Design." *Optics and Photonics News*, vol. 23, no. 6, 2012, pp. 30-35.

51.   Alvarez, Luis W. "Two-element variable-power spherical lens." U.S. Patent No. 3,305,294. 21 Feb. 1967.

52.   Babington, James. "Alvarez Lens Systems: Theory and Applications." *Proc. SPIE, Optical Systems Design 2015: Optical Design and Engineering VI*, vol. 9626, 2015, p. 962615.

53.   Barbero, Sergio. "The Alvarez and Lohmann Refractive Lenses Revisited." *Optics express*, vol. 17, no. 11, 2009, pp. 9376-90.

54.   Barbero, Sergio and Jacob Rubinstein. "Adjustable-Focus Lenses Based on the Alvarez Principle." *Journal of Optics*, vol. 13, no. 12, 2011, p. 125705.

55.   Cai, D. "Higher Order Aberrations of Alvarez Lenses."

56.   Grewe, Adrian et al. "Aberration Analysis of Optimized Alvarez–Lohmann Lenses." *Applied optics*, vol. 53, no. 31, 2014, pp. 7498-506.

57.   Roth, Eckhard et al. "Building Challenging Optical Systems with Alvarez Lenses." *Freeform Optics*, Optical Society of America, 2019, p. FW4B. 6.

58.   Smilie, Paul J et al. "Design and Characterization of an Infrared Alvarez Lens." *Optical Engineering*, vol. 51, no. 1, 2012, p. 013006.

59.   Wu, Rengmao et al. "The Monge-Ampère Equation Design Method and Its Application to Beam Shaping." *Imaging and Applied Optics 2015*, Optica Publishing Group, 2015/06/07 2015, p. FTh3B.1. *OSA Technical Digest (online)*, doi:10.1364/FREEFORM.2015.FTh3B.1.

60.   Shultz, Jason A et al. "Experimental Characterization of Variable Output Refractive Beamshapers Using Freeform Elements." *Proc. SPIE, Laser Beam Shaping XV*, vol. 9194, 2014, p. 91940M.

61.   Suleski, Thomas J et al. "Dynamic Beam Shaping with Freeform Optics." *Proc. SPIE, Laser Beam Shaping XV*, vol. 9194, 2014, p. 91940K.

62.   Zhang, Yaqin et al. "Double Freeform Surfaces Design for Laser Beam Shaping with Monge–Ampère Equation Method." *Optics Communications*, vol. 331, 2014, pp. 297-305.

63.   Wu, Rengmao et al. "Freeform Illumination Design: A Nonlinear Boundary Problem for the Elliptic Monge–Ampére Equation." *Optics letters*, vol. 38, no. 2, 2013, pp. 229-31.

64.   Yang, Lin et al. "Freeform Optical Design of Beam Shaping Systems with Variable Illumination Properties." *Optics express*, vol. 29, no. 20, 2021, pp. 31993-2005, doi:10.1364/OE.436340.

65.   Buchroeder, RA and AS Leonard. "Wide-Field Tilted-Component Telescope: A Leonard Extended Yolo All-Reflecting System." *Applied optics*, vol. 11, no. 7, 1972, pp. 1649-51.

66.   Bauer, Aaron et al. "All-Reflective Electronic Viewfinder Enabled by Freeform Optics." *Optics express*, vol. 27, no. 21, 2019, pp. 30597-605.

67.   Bauer, Aaron et al. "All-Reflective Freeform Viewfinder." *Freeform Optics*, Optical Society of America, 2019, p. FM2B. 4.

68.   Liu, Wenguang et al. "Active Compensation of Low-Order Aberrations with Reflective Beam Shaper." *Optical Engineering*, vol. 53, no. 9, 2014, p. 096103.

69.   Malyak, Phillip H. "Two-Mirror Unobscured Optical System for Reshaping the Irradiance Distribution of a Laser Beam." *Applied optics*, vol. 31, no. 22, 1992, pp. 4377-83.

70.   Ye, Jingfei et al. "Review of Optical Freeform Surface Representation Technique and Its Application." *Optical Engineering*, vol. 56, no. 11, 2017, p. 110901.

71.   Peng, Wei-Jei et al. "Design, Tolerance Analysis, Fabrication, and Testing of a 6-In. Dual-Wavelength Transmission Sphere for a Fizeau Interferometer." *Optical Engineering*, vol. 56, no. 3, 2017, p. 035105.

72.   Beyerlein, Mathias et al. "Dual-Wave-Front Computer-Generated Holograms for Quasi-Absolute Testing of Aspherics." *Applied optics*, vol. 41, no. 13, 2002, pp. 2440-47.

73.   Zhang, Wenlong et al. "Measuring Method of Radius of Curvature Based on Dual-Frequency Laser Interferometer." *Optics and Photonics Journal*, vol. 6, no. 8, 2016, pp. 209-14.

74.   Bielke, Alexander et al. "Model-Based Calibration of an Interferometric Setup with a Diffractive Zoom-Lens." *Proc. SPIE, 2015 International Conference on Optical Instruments and Technology: Optical Systems and Modern Optoelectronic Instruments*, vol. 9618, 2015, p. 961807.

75.   Bielke, Andreas et al. "Fabrication of Aspheric Optics: Process Challenges Arising from a Wide Range of Customer Demands and Diversity of Machine Technologies." *Proc. SPIE, Optical Fabrication, Testing, and Metrology*, vol. 5252, 2004, pp. 1-12.

76.   Bielke, Alexander et al. "Design of a Variable Diffractive Zoom Lens for Interferometric Purposes." *Optical Engineering*, vol. 56, no. 1, 2017, p. 014104.

77.   Bielke, Alexander et al. "Experimental Demonstration of a Diffractive Zoom-Lens for an Interferometric Setup." *Optical Fabrication and Testing*, Optical Society of America, 2014, p. OTu4A. 3.

78.   Dickey, Fred M and Scott C Holswade. *Laser Beam Shaping.* Marcel Dekker New York, 2000.

79.   Rhodes, Patrick W. and David L. Shealy. "Refractive Optical Systems for Irradiance Redistribution of Collimated Radiation: Their Design and Analysis." *Applied optics*, vol. 19, no. 20, 1980, pp. 3545-53, doi:10.1364/AO.19.003545.

80.   Dickey, Fred M. "Laser Beam Shaping." *Optics and Photonics News*, vol. 14, no. 4, 2003, pp. 30-35.

81.   Dickey, Fred M et al. "Laser Beam Shaping Techniques." *Proc. SPIE, High-Power Laser Ablation III*, vol. 4065, 2000, pp. 338-48.

82. Ding, Li et al. "Broadband Beam Shaping Using Two Cascaded Diffractive Optical Elements with Different Sizes of Effective Phase Region." *Proc. SPIE, AOPC 2017: Optoelectronics and Micro/Nano-Optics*, vol. 10460, 2017, p. 1046004.

83. Huang, Xu Guang et al. "High-Efficiency Flat-Top Beam Shaper Fabricated by a Nonlithographic Technique." *Optical Engineering*, vol. 38, no. 2, 1999, pp. 208-13.

84. Veldkamp, Wilfrid B. "Technique for Generating Focal-Plane Flattop Laser-Beam Profiles." *Review of Scientific Instruments*, vol. 53, no. 3, 1982, pp. 294-97.

85. Jozwicki, Romulad. "Beam Shaping in Large Spectral Band for Interferometric Systems." *Proc. SPIE, Interferometry'94: New Techniques and Analysis in Optical Measurements*, vol. 2340, 1994, pp. 273-75.

86. Oliker, Vladimir. "On Design of Free-Form Refractive Beam Shapers, Sensitivity to Figure Error, and Convexity of Lenses." *JOSA A*, vol. 25, no. 12, 2008, pp. 3067-76.

87. Laskin, Alexander and Vadim Laskin. "Beam Shaping to Generate Uniform Laser Light Sheet and Linear Laser Spots." *Proc. SPIE, Laser Beam Shaping XIV*, vol. 8843, 2013, p. 88430C.

88. Laskin, Alexander et al. "Square Shaped Flat-Top Beam in Refractive Beam Shapers." *Proc. SPIE, Laser Beam Shaping XVI*, vol. 9581, 2015, p. 95810K.

89. Laskin, Alexander. "Solutions for Beam Shaping: Control of Laser Intensity Profile and Spot Shape with Refractive Beam Shaping." *Laser Technik Journal*, vol. 10, no. 1, 2013, pp. 37-40.

90. Laskin, Alexander and Vadim Laskin. "Variable Beam Shaping with Using the Same Field Mapping Refractive Beam Shaper." *Proc. SPIE, Laser Resonators, Microresonators, and Beam Control XIV*, vol. 8236, 2012, p. 82360D.

91. Laskin, Alexander and Vadim Laskin. "Freeform Beam Shaping for High-Power Multimode Lasers." *Proc. SPIE, Laser Resonators, Microresonators, and Beam Control XVI*, vol. 8960, 2014, pp. 236-47.

92. Möhl, A et al. "Modular Optical Design for Flexible Beam Shaping of a Top-Hat Profile." *Proc. SPIE, Optical Systems Design 2015: Optical Design and Engineering VI*, vol. 9626, 2015, p. 96261W.

93. Wu, Zhi-Zheng et al. "Laser Beam Shaping with Magnetic Fluid-Based Liquid Deformable Mirrors." *Chinese Physics B*, vol. 26, no. 7, 2017, p. 074201.

94. Hanes, Stephen A et al. "Segmented Mirror Beam Shapers for Creating a Gaussian Intensity Distribution from Uniform Intensity High-Energy Laser Beams." *Proc. SPIE, Laser Beam Shaping V*, vol. 5525, 2004, pp. 104-15.

95. Kleindienst, Roman et al. "Synthetic Design and Integrated Fabrication of Multifunctional Hybrid Beam Shapers." *Proc. SPIE, Laser Beam Shaping XII*, vol. 8130, 2011, p. 81300E.

96. Kukhtarev, Nickolai V et al. "Laser Beam Shaping by Holographic Optical Elements." *Proc. SPIE, Ninth International Conference on Nonlinear Optics of Liquid and Photorefractive Crystals*, vol. 5257, 2003, pp. 152-62.

97. Račiukaitis, Gediminas et al. "Laser Processing by Using Diffractive Optical Laser Beam Shaping Technique." *Journal of laser micro/nanoengineering*, vol. 6, no. 1, 2011.

98. Yang, Jame J and Michael R Wang. "Analysis and Optimization on Single-Zone Binary Flat-Top Beam Shaper." *Optical Engineering*, vol. 42, no. 11, 2003, pp. 3106-13.

99. Yang, Liangxin, et al. "Non-paraxial diffractive and refractive laser beam shaping." *Proc. SPIE, Laser Resonators, Microresonators, and Beam Control XX*, vol. 10518, 2018, 105181Q.

100. Shultz, Jason Allen. "Design, Tolerancing, and Experimental Characterization of Dynamic Freeform Optical Systems." PhD Dissertation, The University of North Carolina at Charlotte, 2017.

101. Bruneton, Adrien et al. "High Resolution Irradiance Tailoring Using Multiple Freeform Surfaces." *Optics express*, vol. 21, no. 9, 2013, pp. 10563-71, doi:10.1364/OE.21.010563.

102. Chen, En-guo et al. "A Laser Beam Shaper for Homogeneous Rectangular Illumination Based on Freeform Micro Lens Array." *Optoelectronics Letters*, vol. 12, no. 4, 2016, pp. 253-56.

103. Chen, Enguo et al. "Design a Freeform Microlens Array Module for Any Arbitrary-Shape Collimated Beam Shaping and Color Mixing." *Optics Communications*, vol. 321, 2014, pp. 78-85.

104. Forbes, Andrew et al. "Wavelength Tunable Laser Beam Shaping." *Optics letters*, vol. 37, no. 1, 2012, pp. 49-51.

105. "Zygo Transmission Sphere Selection Guide." edited by ZYGO, 2014, 4. https://bit.ly/2ZNMqbK.

106. Yang, Pengqian et al. "Transmission Sphere Calibration and Its Current Limits." *Proc. SPIE, Optical Measurement Systems for Industrial Inspection VII*, vol. 8082, 2011, p. 80822L.

107. Gao, Zhishan et al. "Computer-Aided Alignment for a Reference Transmission Sphere of an Interferometer." *Optical Engineering*, vol. 43, no. 1, 2004, pp. 69-74.

108. Peng, Wei-Jei et al. "Design and Tolerance Analysis of a Transmission Sphere by Interferometer Model." *Proc. SPIE, Optical System Alignment, Tolerancing, and Verification IX*, vol. 9582, 2015, p. 958208.

109. Peng, Wei-Jei et al. "Mounting of Reference Surface for a Transmission Sphere." *Proc. SPIE, 8th International Symposium on Advanced Optical Manufacturing and Testing Technologies: Optical Test, Measurement Technology, and Equipment*, vol. 9684, 2016, p. 96840G.

110. Pinto, Joseph. "Transmission Spheres More Than Just a Reference Surface!" *Optifab 2003: Technical Digest*, vol. 10314, 2003, p. 1031415.

111. Dumas, Paul. "Enabling Higher Precision Freeform Surfaces Though Developments in Magnetorheological Finishing (Mrf) and Subaperture Stitching Interferometry (Ssi)." *Renewable Energy and the Environment*, Optical Society of America, 2013/11/03 2013, p. FT3B.1. *OSA Technical Digest (online)*, doi:10.1364/FREEFORM.2013.FT3B.1.

112. Murphy, Paul and Chris Supranowitz. "Freeform Testability Considerations for Subaperture Stitching Interferometry." *Proc. SPIE, Optifab*, vol. 11175, 2019, 111750Z https://doi.org/10.1117/12.2536851.

113. Supranowitz, Chris, et al. "Freeform metrology using subaperture stitching interferometry." *Proc. SPIE, Optics and Measurement International Conference 2016*, vol. 10151, 2016, 101510D.

114. Ohsaki, Yumiko et al. "Interferometer and Interferance Measurement Method." U.S. Patent No. 6,842,255. 11 Jan. 2005.

115. Suzuki, Akiyoshi and Yoshiyuki Sekine. "Interferometer and Interferance Measurement Method." U.S. Patent No. 7,106,455. 12 Sep. 2006.

116. Lohmann, Adolf W. "A New Class of Varifocal Lenses." *Applied optics*, vol. 9, no. 7, 1970, pp. 1669-71.

117. Burge, James H. "Fizeau Interferometry for Large Convex Surfaces." *Proc. SPIE, Optical Manufacturing and Testing*, vol. 2536, 1995, pp. 127-38.

118. Alfano, Robert R. "The Supercontinuum Laser Source." *The Supercontinuum Laser Source: The Ultimate White Light, ISBN 978-1-4939-3324-2. Springer Science+ Business Media New York*, 2016.

119. "Fizeau Interferometer for Optical Testing." LightTrans Gmbh 2021 https://www.lighttrans.com/use-cases/application-use-cases/fizeau-interferometer-for-optical-testing.html. Accessed July 24, 2021.

120. Granzow, Nicolai. "Supercontinuum White Light Lasers: A Review on Technology and Applications." *Proc. SPIE, Joint TC1 - TC2 International Symposium on Photonics and Education in Measurement Science 2019*, vol. 11144, SPIE, 2019. https://doi.org/10.1117/12.2533094.

121. Singh, Manisha et al. "Beam Shaping of Supercontinuum Pulses." *Proc. SPIE, Optical Systems Design 2015: Optical Design and Engineering VI*, vol. 9626, 2015, p. 962633.

122. Herráez, Miguel Arevallilo et al. "Fast Two-Dimensional Phase-Unwrapping Algorithm Based on Sorting by Reliability Following a Noncontinuous Path." *Applied optics*, vol. 41, no. 35, 2002, pp. 7437-44.

123. Zhao, Zixin et al. "Robust 2d Phase Unwrapping Algorithm Based on the Transport of Intensity Equation." *Measurement Science and Technology*, vol. 30, no. 1, 2018, p. 015201.

124. Gray, Robert. "Zernikecalc." 2021. https://www.mathworks.com/matlabcentral/fileexchange/33330-zernikecalc.

125. Lakshminarayanan, Vasudevan and Andre Fleck. "Zernike Polynomials: A Guide." *Journal of Modern Optics*, vol. 58, no. 18, 2011, p. 1678, doi:10.1080/09500340.2011.633763.

126. Koerber, Jonathan et al. "Reduction of Retrace Error from Broadband Variable Transmission Spheres in Fizeau Interferometry." *Optics Continuum*, 2022, doi:https://doi.org/10.1364/OPTCON.458860.

127. Koerber, Jonathan et al. "Broadband Variable Transmission Sphere for Fizeau Interferometry." *Optics*, vol. 3, no. 1, 2022, pp. 88-98, https://www.mdpi.com/2673-3269/3/1/11.

128. Koerber, Jonathan and Thomas J Suleski. "Design of a Broadband Variable Transmission Sphere." *Frontiers in Optics*, Optical Society of America, 2020, p. FM1A. 7.

129. He, Yiwei et al. "Modeling Fizeau Interferometer Based on Ray Tracing with Zemax." *Proc. SPIE, AOPC 2015: Optical Test, Measurement, and Equipment*, vol. 9677, 2015, p. 96770G.

130. Huang, Chunsheng. "Propagation Errors in Precision Fizeau Interferometry." *Applied optics*, vol. 32, no. 34, 1993, pp. 7016-21, doi:10.1364/AO.32.007016.

131. Kreischer, Cody B. "Retrace Error: Interferometry's Dark Little Secret." *Proc. SPIE, Optifab 2013*, vol. 8884, 2013, p. 88840X.

132. Geary, Joseph et al. "Retrace Error: A Case Study." *Proc. SPIE, San Diego 1992*, vol. 1776, 1992, https://doi.org/10.1117/12.139232.

133. Han, Sen and Erik Novak. "Retrace Error for the Measurement of a Long-Radius Optic." *Proc. SPIE, ICO XVIII 18th Congress of the International Commission for Optics*, vol. 3749, 1999, https://doi.org/10.1117/12.354906.

134. "User Manual." *Zemax OpticStudio 22.1*, 2022, p. 1091.

135. Romero, Louis and Fred M Dickey. "What Makes a Beam Shaping Problem Difficult." Sandia National Labs., 2000.

136. Duerr, Fabian and Hugo Thienpont. "Direct Design of Laser-Beam Shapers, Zoom-Beam Expanders, and Combinations Thereof." *Proc. SPIE, Optical Design and Testing VII*, vol. 10021, 2016, p. 100210K.

137. Hoffnagle, John A and C Michael Jefferson. "Beam Shaping with a Plano-Aspheric Lens Pair." *Optical Engineering*, vol. 42, no. 11, 2003, pp. 3090-99.

138. Laskin, Alexander and Vadim Laskin. "Refractive Field Mapping Beam Shaping Optics: Important Features for a Right Choice." *International Congress on Applications of Lasers & Electro-Optics*, vol. 2010, Laser Institute of America, 2010, pp. 1181-89.

139. Laskin, Alexander and David Shealy. "Designing Refractive Beam Shapers Via Aberration Theory." *Proc. SPIE, Laser Beam Shaping XV*, vol. 9194, 2014, p. 91940T.

140. Laskin, Alexander et al. "Applying Refractive Beam Shapers in Creating Spots of Uniform Intensity and Various Shapes." *Proc. SPIE, Laser Resonators and Beam Control XII*, vol. 7579, 2010, p. 75790N.

141. Shealy, David L and Shao-Hua Chao. "Geometric Optics-Based Design of Laser Beam Shapers." *Optical Engineering*, vol. 42, no. 11, 2003, pp. 3123-38.

142. Shealy, David L and John A Hoffnagle. "Design and Analysis of Plano-Aspheric Laser Beam Shapers." *Proc. SPIE, Laser Beam Shaping XIII*, vol. 8490, 2012, p. 849003.

143. Shealy, David L and John A Hoffnagle. "Laser Beam Shaping Profiles and Propagation." *Applied optics*, vol. 45, no. 21, 2006, pp. 5118-31.

144. Hoffnagle, John A and David L Shealy. "Optical and Mechanical Tolerances for Two-Lens Plano-Aspheric Laser Beam Shapers." *Proc. SPIE, Laser Beam Shaping XIII*, vol. 8490, 2012, p. 849004.

145. ten Thije Boonkkamp, J. H. M. et al. "The Monge-Ampère Equation for Freeform Optics." *Imaging and Applied Optics 2015*, Optica Publishing Group, 2015/06/07 2015, p. FTh3B.4. *OSA Technical Digest (online)*, doi:10.1364/FREEFORM.2015.FTh3B.4.

146. Jiang, Wu et al. "Design and Testing of a Refractive Reshaping System." *Proc. SPIE, 1993 International Symposium on Optics, Imaging, and Instrumentation*, vol. 2000, 1993, OP. https://doi.org/10.1117/12.163670.

147. Zhang, S. et al. "Single-Element Laser Beam Shaper for Uniform Flat-Top Profiles." *Optics express*, vol. 11, no. 16, 2003, pp. 1942-48, doi:10.1364/OE.11.001942.

148. Smilie, Paul Joseph. "Dynamic Optical Systems through Laterally Translated Refractive Freeform Elements." University of North Carolina at Charlotte, 2011.

149. Mann, Klaus R et al. "Characterization of Excimer Laser Beam Parameters." *Proc. SPIE, Third International Workshop on Laser Beam and Optics Characterization*, vol. 2870, 1996, pp. 367-77.

150. ISO. "Optics and Photonics - Lasers and Laser-Related Equipment - Test Methods for Laser Beam Power (Energy) Density Distribution." vol. 13694, 2018.